

RADIOMETRIC DESIGN AND ANALYSIS OF THE BREAKTHROUGH STARSHOT  
INITIATIVE IN LAUNCH SPACE

by

Joseph Rice

---

Copyright © Joseph Rice 2020

A Thesis Submitted to the Faculty of the

JAMES C. WYANT COLLEGE OF OPTICAL SCIENCES

In Partial Fulfillment of the Requirements

For the Degree of

MASTER OF SCIENCE

In the Graduate College

THE UNIVERSITY OF ARIZONA

2020

THE UNIVERSITY OF ARIZONA  
GRADUATE COLLEGE

As members of the Master's Committee, we certify that we have read the thesis prepared by **Joseph Allen Rice**, titled *Radiometric Design and Analysis of the Breakthrough Starshot Initiative in Launch Space* and recommend that it be accepted as fulfilling the thesis requirement for the Master's Degree.

  
\_\_\_\_\_  
*Professor Michael Hart, Chair*

Date: May 13, 2020

  
\_\_\_\_\_  
*Professor Daewook Kim*

Date: 5-13-2020


  
\_\_\_\_\_  
*Professor J. Roger P. Angel*

Date: May 13, 2020

Final approval and acceptance of this thesis is contingent upon the candidate's submission of the final copies of the thesis to the Graduate College.

I hereby certify that I have read this thesis prepared under my direction and recommend that it be accepted as fulfilling the Master's requirement.

  
\_\_\_\_\_  
*Professor Michael Hart*  
Master's Thesis Committee Chair  
*Wyant College of Optical Sciences*

Date: 5/28/2020 

ARIZONA

## **ACKNOWLEDGEMENTS**

I would like to first thank my advisor, Michael Hart, for not only guiding me through the research process that has made this work possible, but also for the many opportunities over the last four years as a member of his Adaptive Optics research group. The conferences attended and projects I've be fortunate enough to work on as a result have helped shape my growing knowledge of optics as a whole and pointed me on a path forward for the future. For this and the many memories, I am very appreciative

I would also like to thank Dae Wook Kim and the many other professors I have gotten the chance to work with. The research experiences have proved invaluable both personally and professionally. I thank all the members of the AO research group who I've worked alongside over the years and become friends with in the process. I also would like to acknowledge and thank the Breakthrough Initiatives as well as the Starshot Committee for supporting this work.

Finally, I am thankful to my family for their continued support, to God for everything I have been blessed with, and to all of the friends I've come to know throughout my years at the University of Arizona. My experience here has been one I will always be grateful for.

# TABLE OF CONTENTS

<b>LIST OF FIGURES.....</b>	<b>5</b>
<b>LIST OF TABLES.....</b>	<b>6</b>
<b>ABSTRACT.....</b>	<b>7</b>
<b>1. INTRODUCTION.....</b>	<b>8</b>
<b>2. WAVE-FRONT SENSING.....</b>	<b>9</b>
2.1 Need for Wave-Front Sensing.....	9
2.2 Guide Beacon Architectures.....	10
2.3 Need for Radiometric Modeling.....	12
<b>3. KINEMATIC MODEL.....</b>	<b>14</b>
3.1 Previous Research and Modeling.....	14
3.2 Model Structure.....	15
3.3 Initial Conditions.....	21
3.4 Model Results.....	22
3.5 Comparisons to Previous Research.....	24
<b>4. PROPAGATION MODEL.....</b>	<b>25</b>
4.1 Previous Research and Modeling.....	25
4.2 Model Structure.....	26
<b>5. TRADE STUDY PARAMETERS.....</b>	<b>38</b>
5.1 Constant Drive Space Parameters.....	38
5.2 Varied Launch Space Parameters.....	39
<b>6. TRADE STUDY RESULTS.....</b>	<b>43</b>
6.1 System Overview.....	43
6.2 Gaussian PSF.....	44
6.3 Donut PSF.....	47
6.4 Four-Lobed PSF.....	50
6.5 Implications on System Design.....	53
<b>7. CONSIDERATIONS FOR FUTURE WORK AND CONCLUSIONS.....</b>	<b>55</b>
<b>8. REFERENCES.....</b>	<b>57</b>

## LIST OF FIGURES

Figure 1. – Concept for the launch projector.....	9
Figure 2. – Basic AO architecture with high energy laser (HEL), wave-front sensor (WFS), AO correction, and deformable mirror.....	10
Figure 3. – Diagram of projector and nanocraft geometry in relation to one another, accounting for both the Earth’s rotation as well as dynamic change in point ahead vector.....	11
Figure 4. – Guide beacon architecture geometry, with isoplanatic angle shown in relation to mothership and nanocraft.....	12
Figure 5. – Kinematic model architecture as a series of iterative equations.....	16
Figure 6. – Kinematic model outputs.....	22
Figure 7. – Preliminary irradiance profiles generated in FRED.....	26
Figure 8. – Basic geometric layout of system propagation.....	27
Figure 9. – Sail in propagation model.....	28
Figure 10. – Geometry of sail reflection. The dA area element is off-axis with the incoming beam on-axis.....	29
Figure 11. – Unfiltered von Karman turbulence.....	32
Figure 12. – Filtered von Karman turbulence.....	33
Figure 13. – Unfiltered and filtered power spectrum.....	34
Figure 14. – Incident PSF profiles on sail.....	35
Figure 15. – Reflected PSF profiles back towards projector.....	37
Figure 16. – BRDF of Kapton polyimide.....	39
Figure 17. – Diffraction limited Gaussian PSF at start of launch.....	40
Figure 18. – Diffraction limited donut PSF at start of launch.....	41
Figure 19. – Diffraction limited four-lobed PSF at start of launch.....	42
Figure 20. – Incident and reflected power at several Strehl ratios for Gaussian PSF.....	44
Figure 21. – Incident and reflected irradiance profiles at 70% Strehl for Gaussian PSF.....	46
Figure 22. – Incident and reflected power at several Strehl ratios for donut PSF.....	47
Figure 23. – Incident and reflected irradiance profiles at 70% Strehl for donut PSF.....	49
Figure 24. – Incident and reflected power at several Strehl ratios for four-lobed PSF.....	50
Figure 25. – Incident and reflected irradiance profiles at 70% Strehl for four-lobed PSF.....	52

## LIST OF TABLES

Table 1. – Definitions of initial conditions for kinematic model.....	16
Table 2. – Definitions of calculated variables for kinematic model.....	20
Table 3. – Values of initial conditions for kinematic model.....	21
Table 4. – Values of initial conditions for propagation model.....	28
Table 5. – Summary of AO performance and power breakdown.....	43
Table 6. – Summary of incident and reflected power at several Strehl ratios for Gaussian PSF.....	45
Table 7. – Summary of incident and reflected power at several Strehl ratios for donut PSF.....	48
Table 8. – Summary of incident and reflected power at several Strehl ratios for four-lobed PSF.....	51
Table 9. – Resulting wave-front error in measurement for Gaussian PSF.....	54
Table 10. – Resulting wave-front error in measurement for donut PSF.....	54
Table 11. – Resulting wave-front error in measurement for four-lobed PSF.....	54

## ABSTRACT

The Breakthrough Starshot Initiative is a project that aims to send a nanocraft to the Proxima Centauri system. The nanocraft will deploy a solar sail driven by a 100 GW laser beam at 1064 nm projected from a segmented aperture of several kilometers in diameter<sup>1</sup>. Adaptive Optics (AO) will be implemented to facilitate the transfer of energy efficiently and effectively<sup>2</sup>. The AO system will need a guide beacon for wave-front measurements, and there are multiple architectures being investigated. One such architecture involves the use of reflected drive light as a beacon. As a result, it is imperative to quantify the nature of the system's radiometric response.

A model has been developed for the examination of radiometric properties pertaining to the Starshot system. The complete radiometric model uses two MATLAB models, referred to as the kinematic model and propagation model, for a robust analysis. The kinematic model predicts the nanocraft's motion while the propagation model quantifies and characterizes the light returning from the sail. Outputs from the kinematic model include craft position, velocity, and acceleration at any time throughout the duration of the launch. Outputs from the propagation model include power and irradiance maps incident upon the sail and reflected back toward the launch projector at multiple craft positions.

The greater Starshot system can be broken down into two parameter spaces: launch space and drive space. The launch space consists of the launch projector and Earth's atmosphere while drive space consists of the sail itself. For the purposes of this study, the drive space parameters (i.e., sail shape, BRDF, absorptance/reflectance, etc.) are fixed. The exact values of these variables are chosen based on current Starshot estimates and congruent research. Instead, this study focuses on the launch space parameters. The primary parameter to consider here is the shape of the PSF of the outgoing beam from the launch projector and the implications this shape will have on wave-front sensing. The shapes chosen for simulating are consistent with those being currently investigated for optimizing sail stability: Gaussian, donut, and four-lobed.

With each specified system configuration, the model outputs have been generated leading to a study of which launch space configuration (i.e., PSF shape) is optimal for wave-front sensing. Atmospheric turbulence is simulated using the propagation model and different levels of atmospheric correction are applied in an effort to base-line the requirements that will need to be imposed on the future AO system. A trade study detailing these findings is provided.

# 1. INTRODUCTION

The Breakthrough Starshot Initiative intends to utilize photon drive light from a large laser array of segmented apertures, referred to as the launch projector, in conjunction with a highly reflective solar sail as a means of interstellar travel<sup>1</sup>. A small craft equipped with sensors, referred to as the nanocraft, will be attached to the sail in hopes of retrieving some information about its desired destination, Proxima Centauri b. Each nanocraft and sail will be released into the path of the beam from a mothercraft in orbit around Earth. In order to achieve such a feat on the scale of a lifetime, the project's goal is to accelerate the nanocraft up to 20% the speed of light over the course of 600 s.

The project as a whole is still in its foundational stages, and as such there are many unknowns when it comes to system parameters. Specifics regarding the overall design of the system, such as the beam shape, method of beam steering, launch projector architecture, sail shape and material, etc. are not yet determined. In general, system requirements are only recently being established and thus many research efforts revolve around simply obtaining baseline figures to start with, as is the case with this study. However, there are certain parameters that are agreed upon as starting points for research efforts. These parameters will be held constant for the purposes of this study.

Estimates in the project's early phases indicate that the launch projector will be roughly 4 km in diameter. This projector will be broken down into many smaller sub-apertures. A concept for the projector developed by Noyes is shown in Figure 1<sup>3</sup>. The beam is assumed to operate at a wavelength of 1064 nm, a wavelength at which the atmosphere is relatively transparent and thus efficient for energy transfer. The sail will be roughly 4 m in diameter and have a mass of approximately 1 g<sup>1</sup>.

Aside from the parameters discussed above, there are few other parameters that have been decided upon. Research groups have been commissioned to investigate different sub-systems of the overall Starshot project. This study focuses on identifying the appropriate system architecture for maximizing performance of the wave-front sensing sub-system. In particular, the radiometric properties of the system are considered in an effort to characterize the quantity of reflected drive light as a function of varying launch space parameters.

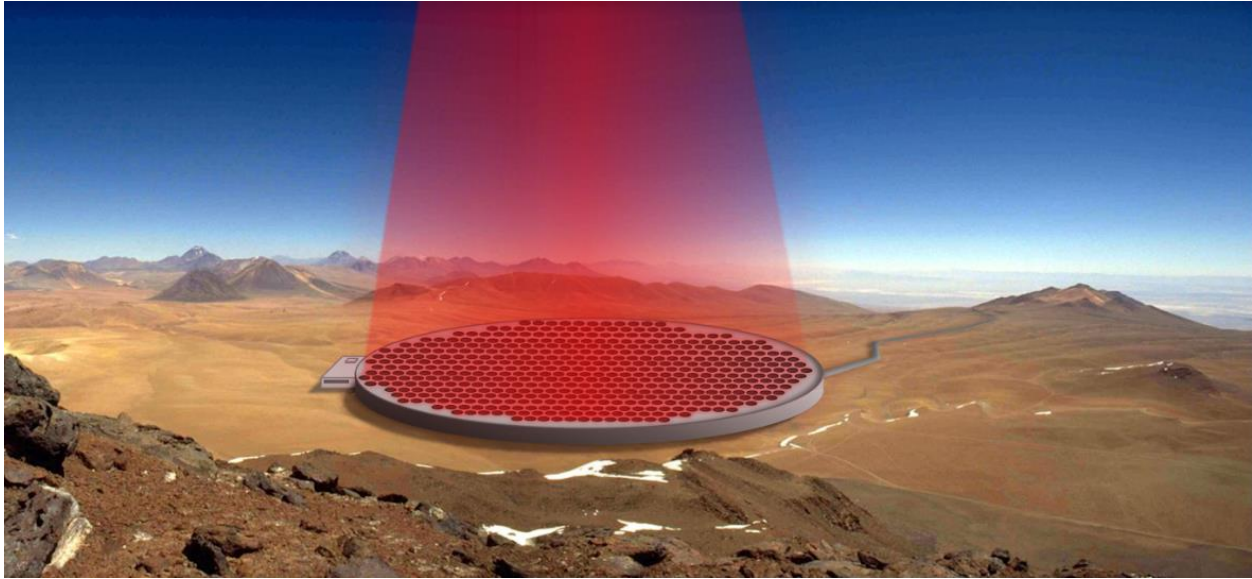


Figure 1. Concept for the launch projector<sup>3</sup>.

## 2. WAVE-FRONT SENSING

### 2.1 Need for Wave-Front Sensing

In order to accelerate the nanocraft to 20% the speed of light in 600 s the drive light needs to be coupled to the nanocraft's solar sail as efficiently as possible, despite constant fluctuations in the Earth's atmosphere that will cause phase errors across the segments of the launch projector as well as piston shifts between them<sup>2</sup>. Without correcting for these fluctuations, the system risks losing great amounts of energy due to atmospheric turbulence. A measurement of the errors must occur prior to correction, and the intention is to accomplish this using wave-front sensing. As such, wave-front sensing will be fundamental to the success of the Starshot project.

Wave-front sensing is commonly used in AO systems as a means of measuring the phase errors across a pupil introduced by turbulent media in layers of the atmosphere. In general, a feedback loop is used in conjunction with corrector elements, such as a deformable mirror (DM) with actuators, to compensate for the measured errors in real time. A basic diagram outlining the architecture is displayed in Figure 2. These systems are often used on Earth based telescopes for astronomical observation. However, in the case of the Starshot system the desired wavefront will be exiting, not entering, the atmosphere. Despite the reversal in system orientation, the general premise of wave-front detection and correction is the same. Correction will be applied at the launch

aperture to provide a beam that is phased upon leaving the atmosphere. Accordingly, fast wave-front sensing with feedback to adaptive corrector elements in the projector optics will be used to minimize atmospheric effects and maximize power incident on the sail<sup>2</sup>.

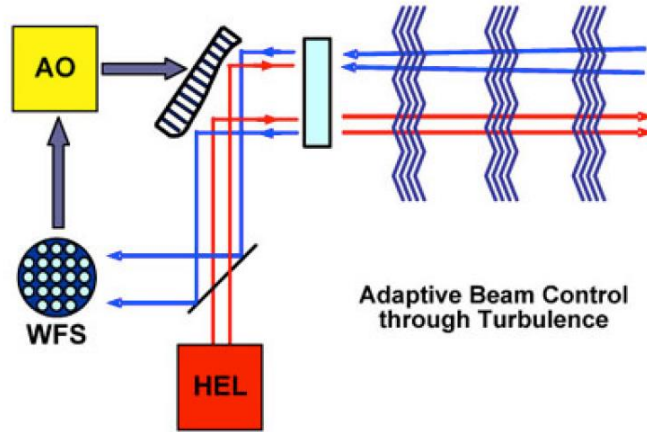


Figure 2. Basic AO architecture with high energy laser (HEL), wave-front sensor (WFS), AO correction, and deformable mirror.

To achieve accurate wave-front sensing there must be a reference beacon of some kind to make the measurement with. This reference beacon can be natural or artificial depending on the circumstances. In the case of Starshot, a natural beacon in the form of starlight will not be suitable. This is because there will not be any stars sufficiently bright and close enough to the nanocraft's line of sight. Many AO systems make use of artificial laser guide stars (LGS), but LGS suffer from tilt indeterminacy that make them non-ideal for the precision required. Additionally, the prospect of using Rayleigh scattered light from the launch projector has been suggested. However, the drive light will not focus in the sky and thus distinguishing it from the return light is not feasible<sup>2</sup>. Instead, there are other guide beacon architectures of interest.

## 2.2 Guide Beacon Architectures

One proposition for a guide beacon architecture would utilize the reflected drive light from the sail itself as the beacon<sup>4</sup>. This is particularly desirable as the reflected drive light will always be very close to the nanocraft's line of sight. It is also worth noting that, as mentioned previously, there will be piston differences between the sub-apertures. This is due to the likely non-trivial spatial separation between each aperture. Reflected drive light can be used to measure these errors as it will have sufficient spatial coherence across the launch aperture. Despite these benefits, initially it appears that the reflected drive light approach is not entirely ideal, as the nanocraft's instantaneous

velocity vector will not be directly aligned with the line of sight from the projector's frame of reference. The rotation of the Earth leads to apparent orbital motion of the nanocraft from the projector's frame of reference, causing this effect. This could be problematic, as one has to point ahead of the nanocraft in order to compensate for the beam's time of flight. Figure 3 illustrates the effect. However, upon inspection it is found that the point-ahead angle is always smaller than the isoplanatic angle. This implies that the reflected drive light can in fact be used for effective wave-front sensing wherever possible<sup>2</sup>. After approximately the first 30 s of launch the reflected drive light should be Doppler shifted on the order of 10 nm. This would be enough separation in wavelength from the initial drive light for a dichroic beam splitter to pick off the reflected drive light for use in wave-front sensing. However, in the first 30 s of launch the light will not be separated sufficiently. In this regime the reflected drive light will be lost in the atmospheric backscatter from the initial drive light. To deal with this effect a different approach will have to be used here.

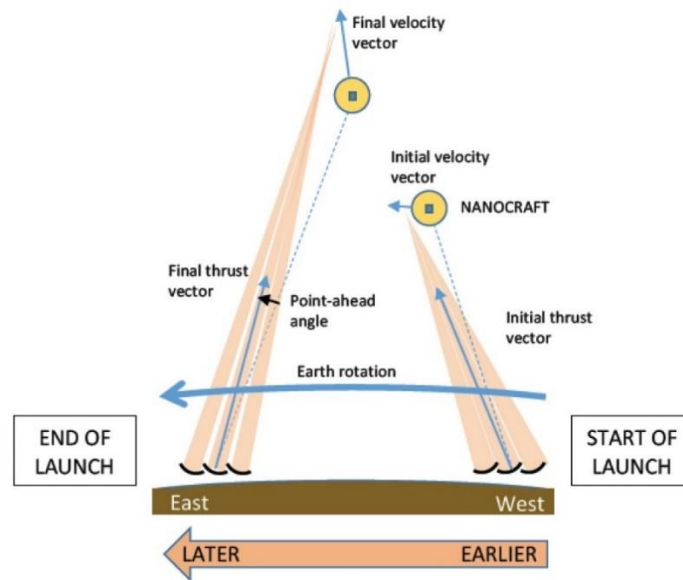


Figure 3. Diagram of projector and nanocraft geometry in relation to one another, accounting for both the Earth's rotation as well as dynamic change in point ahead vector<sup>2</sup>.

For the first 30 s of launch an additional artificial beacon that emits at a separate wavelength from the drive wavelength will be needed. One proposal involves using a beacon on-board the mothercraft. The mothercraft's orbit would ideally allow for the beacon to hang within the launch projector's isoplanatic patch for the full 30 s. The orbit required for such an architecture to be successful while only using one mothercraft has been determined by Noyes<sup>3</sup>. Another proposition

would use multiple beacons on-board satellites that also hang within the isoplanatic patch for the full 30 s.

It is worth noting that there has also been the suggestion of an artificial beacon on-board the nanocraft itself<sup>2</sup>. However, this architecture would take up valuable space on the nanocraft that could otherwise be used for additional scientific purposes. The benefits of this approach are very similar to those of the reflected drive light, and the radiometric response of the system would not be as crucial to its performance. Thus, this architecture is not considered here.

The most likely guide beacon architecture makes use of a two-fold approach, utilizing different beacons at different points in the launch. This system layout is shown in Figure 4, where  $\theta_0$  is the isoplanatic angle and  $\alpha$  is the angle between the mothership and the nanocraft's line of site. The distance  $Z_{LGS}$  is the distance to the mothership while  $Z_{nano}$  is the distance to the nanocraft. As denoted, the angle between the two crafts is smaller than the isoplanatic angle, making a beacon on-board the mothership viable in the first 30 s. As such, for the first 30 s an artificial beacon, likely on-board the mothercraft, would be implemented. After the first 30 s the reflected drive light would serve as the guide beacon. With this in mind, the radiometric response of the system under varying conditions becomes critical to the architecture's success.

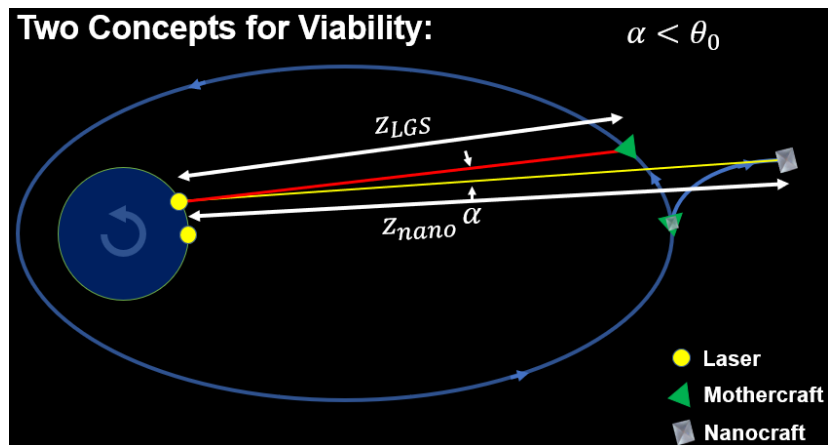


Figure 4. Guide beacon architecture, with isoplanatic angle shown in relation to mothership and nanocraft<sup>3</sup>.

### 2.3 Need for Radiometric Modeling

As discussed, the reflected drive light is of particular interest as a prospect for the system's guide beacon after the first 30 s of launch. While this architecture has many benefits, it can only be

implemented if the magnitude of light reflected directly back towards the launch projector is in the regime of what is required for accurate wave-front sensing. Essentially, if the reflected drive light is too faint from the projector's frame of reference, it cannot be utilized. This is the problem many AO systems encounter with an overwhelming majority of stars in the sky. As such, one of the first steps in deciding whether or not this architecture can succeed involves simulating the amount of light that returns to the projector.

This simulation must take into account the whole system, as there are many factors that can change the overall radiometric properties. In both launch space and drive space there are parameters of interest. As mentioned, for the purposes of this study the drive space parameters are fixed. This implies that the sail shape, bi-directional reflectance distribution function (BRDF), reflectance/absorptance, etc. are set to one fixed value each. There is a congruent study documented in the work by Bowers that considers the effects of varying these parameters on the radiometric response<sup>5</sup>. Instead, here the launch space parameters are varied. The key parameter of interest is the PSF shape of the beam. Thus, the amount of reflected drive light that returns to the projector must be characterized as a function of varying PSF shape.

The atmosphere must also be considered in this simulation. While an AO system will be used to create a beam that is as close to diffraction limited as possible, the limits of what is required from this system are not yet known. Depending on the AO performance achieved, there will be a residual speckle from the atmospheric turbulence that modulates the ideal output beam. It follows that this residual will have an effect on the amount of return drive light. If the beam is highly aberrated, less light will be likely to reach the sail and thus the return light will drop in magnitude. This can in effect turn a beacon that would nominally be useful for wave-front sensing into one that is not. By studying what levels of AO correction give adequate amounts of return light, a benchmark on AO system performance can be set. There are other factors that may also set requirements on AO performance. For instance, sail stability is a key figure of merit for success. If a sail is unstable due to random incident speckle, it may fly off course and result in an unwanted trajectory. While this is certainly an important feature to consider, sail stability is not inherently incorporated into this model. However, there is ongoing work examining this phenomenon in further detail<sup>6</sup>.

Simulating the quantity of return light as a function of varying PSF shape and AO system performance is key in characterizing the feasibility of using reflected drive light as the guide beacon. There are a few cornerstone parameters needed prior to running the propagation model that will actually estimate the reflected light. Namely, a range of distances over which the launch will occur, as well as an amount of incident power on the sail required to achieve the desired propulsion (i.e.  $0.2c$  in 600 s) are of interest. The range of distances will allow for a complete radiometric characterization at any point in the launch duration. The power requirement will help with modeling AO performance, as it will allow for an estimation of Strehl ratio for any given starting power at the projector, and therefore an allowable residual turbulence. In order to generate these parameters, a kinematic model for simulating the nanocraft's motion is needed.

### **3. KINEMATIC MODEL**

#### **3.1 Previous Research and Modeling**

The kinematics of interstellar travel while using a photon drive have been studied and characterized in prior work. In particular, the Breakthrough Starshot Initiative has commissioned for preliminary modeling of the system kinematics by Parkin. Parkin reports his findings in his paper "The Breakthrough Starshot System Model", and bases many of his assumptions and physics from previous research conducted by Kulkarni<sup>1</sup>. In Kulkarni's paper "Relativistic Spacecraft Propelled by Direct Energy" the foundations for modelling the kinematic motion of spacecraft such as Starshot's nanocraft are formulated<sup>7</sup>. In particular, the relativistic nature of the system is given detailed consideration.

Kulkarni essentially provides equations for the motion of the nanocraft that allow for quantities such as position, velocity, and acceleration to be calculated at any point in time. These equations relate the differences between the launch projector's reference frame and the nanocraft's reference frame via the Lorentz factor. Thus, relativity is accounted for throughout the duration of the launch. Parkin takes this foundation provided by Kulkarni and adds a formulation for the beam incident upon the sail. This provides a model that is much closer in approximation to the Starshot system. Parkin also considers effects such as sail thermal re-emission of absorbed beam energy and the potential of sail transmittance in his model. Parkin's model is convenient to use as a backbone for the kinematic model in this study as it expands upon legacy research while providing a more robust

simulation. It is also commonly cited and referred to by the Breakthrough Starshot project as a whole, making it a good starting point for many different research groups.

One additional convenience of using Parkin's model is that the results of the kinematic model in this study can be compared to those of Parkin. For example, there are several assumptions about quantities such as starting projector-to-sail distance and atmospheric loss due to scattering and absorption that Parkin makes. In this study these parameters are slightly different in value due to more recent research, but the kinematic equations are the same as those used by Parkin. As a result, a side-by-side comparison demonstrates similar trends in how the system evolves with time, but important distinctions in the magnitude of several quantities.

### **3.2 Model Structure**

The kinematic model uses the equations adapted by Parkin from Kulkarni to calculate all parameters of interest. The model is built in MATLAB using an algorithm that loops over small, defined time steps on the order of 1  $\mu$ s. It then stores the desired values over larger intervals to provide both accurate and efficient computation. The key parameters of interest for use as inputs to the propagation model that follows are the range of projector-to-nanocraft distances and the required power incident on the sail. However, many other quantities, such as force on sail, are also stored for use in comparisons to Parkin's model as well as potentially for other adjacent research.

The iterative process begins with a set of initial conditions. These are the few quantities that are relatively well agreed upon and thus make for the best starting points. Once received, the calculations then follow the process outlined by the flow chart in Figure 5. The initial conditions displayed on the left of the chart are then further defined in Table 1. Several of the calculated quantities use input values from both the initial conditions, as well as from other variables calculated upstream. This is why there are arrows coming from multiple locations to some of the variables. The box in the bottom left of Figure 5 keeps track of how many compounded computations are required for each variable. The results cache simply stores the final values of each calculated variable at the end of every iteration cycle.

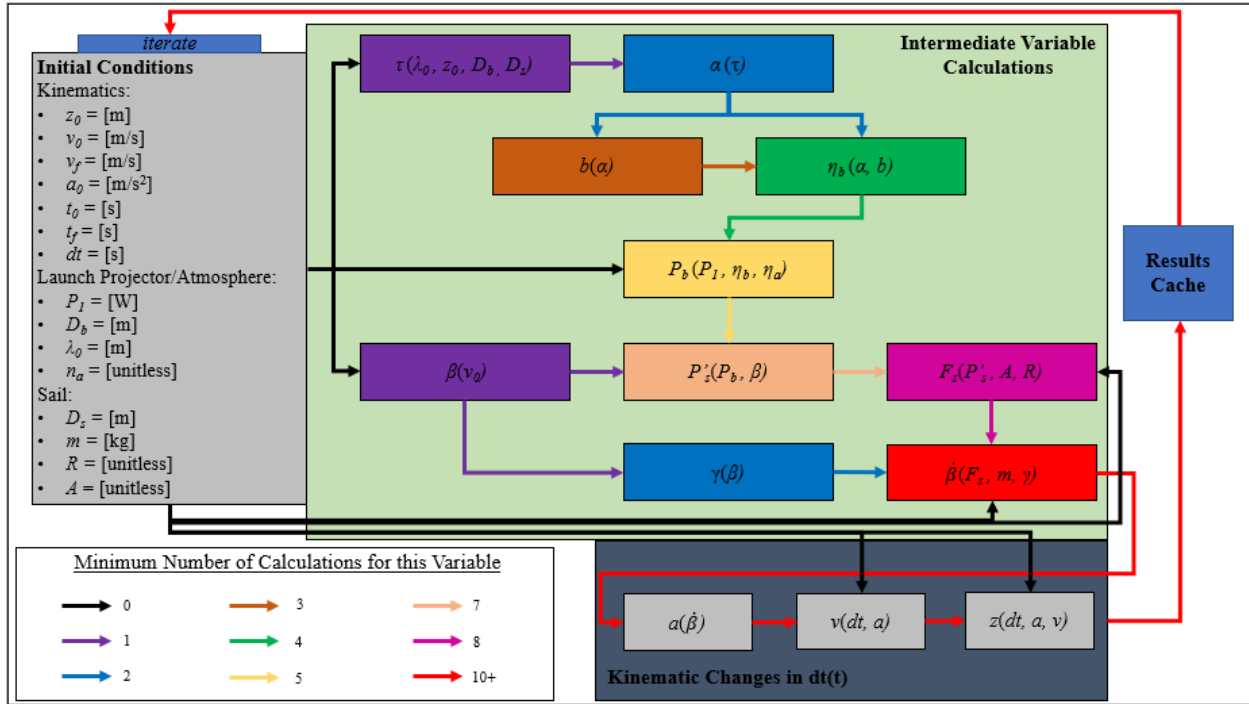


Figure 5. Kinematic model architecture as a series of iterative equations.

Table 1. Definitions of initial conditions for kinematic model.

Variable	Definition
$z_0$	Nanocraft's initial distance from projector
$v_0$	Nanocraft's initial velocity
$v_f$	Nanocraft's final velocity
$a_0$	Nanocraft's initial acceleration
$t_0$	Time at start of launch
$t_f$	Time at end of launch
$dt$	Time step in-between calculations
$P_1$	Power at projector
$D_b$	Projector diameter
$\lambda_0$	Wavelength of drive light at projector
$n_a$	Loss due to atmospheric scattering and absorption
$D_s$	Sail diameter
$m$	Nanocraft mass
$R$	Sail reflectance
$A$	Sail absorptance

The series of calculations is illustrated by Parkin in his model and begins with the given set of input parameters described in Table 1. First, a beam transfer efficiency ( $\eta_b$ ) must be determined. The beam transfer efficiency is a fractional term that is multiplied by the total power at the projector ( $P_1$ ) to account for power lost during propagation due to non-atmospheric effects. When considering the beam transfer efficiency for the Starshot system, one must recognize the fact that the beam will really be operating in two regimes. Initially, the beam is concentrated primarily on the sail and thus the majority of power is delivered to the sail. This implies the beam transfer efficiency is high here. However, as a result of the launch projector's diffraction limit, at a certain distance the beam will actually begin to overflow and spill off of the sail. Resultingly, less and less power is actually delivered to the sail as the projector-to-nanocraft distance increases. This implies the beam transfer efficiency is lower here. The fact that the beam transfer efficiency evolves as a function of time must be accounted for and is done so using the concept of Goubau beams.

The beam transfer efficiency used in both Parkin's system model as well as the kinematic model here is adapted by Parkin from the work by Goubau on Goubau beams<sup>8</sup>. Goubau beams are a concept used in microwave antennae free space transmission. The beams essentially resemble a Gaussian beam when high transfer efficiency is needed and a top-hat beam when lower transfer efficiency is needed. Actual beam quality is idealized in each regime it operates in. The beam is a mathematical construct in the context of this study, but it allows for simulating the effect beam fall-off has on the power transferred to the sail as the projector-to-nanocraft distance increases. Even though the actual projector beam does not undergo a physical shape transformation, the transfer efficiency behaves as if the beam were doing so because of the overflowing effects. By incorporating the beam transfer efficiency of a Goubau beam this effect is captured. Using this logic, Parkin generated a beam transfer efficiency, based on Goubau beams, that depicts what is physically occurring in the plane of the sail.

The transfer efficiency is ultimately a function of a single dimensionless parameter ( $\tau$ ). Using the wavelength of drive light at the projector ( $\lambda_0$ ), the nanocraft's initial distance from the projector ( $z_0$ ), and the projector and sail diameters ( $D_b$  and  $D_s$ ),  $\tau$  can be calculated at the starting time ( $t_0$ ) as given by Equation 1. One notices that immediately the fall-off effect is being incorporated, as the equation essentially gives the size of the airy disk core at the sail divided by the sail size. This

can be thought of as a sail fill factor governing how much of the airy disk core is actually incident upon the full sail.

$$\tau = \frac{8\lambda_o z}{D_s D_b} \quad (1)$$

The result from Equation 1 is used to calculate two more dimensionless parameters ( $\alpha$  and  $b$ ). This is shown by Equations 2-3. Then, the beam transfer efficiency is calculated. There is no closed-form solution, so a numerical approximation is used. This approximation can take on two values ( $\eta_1$  or  $\eta_2$ ), and Equations 4-6 outline this. These parameters all work together in order to actually draw the distinction between the two regimes (i.e. underfilled and overfilled sail as a result of beam fall-off) as discussed earlier. As  $\tau$  increases, implying the projector-to-nanocraft distance is increasing,  $\alpha$  decreases. The numerical approximation is driven by  $\alpha$ . Once  $\alpha$  reaches a certain threshold, determined by Parkin, the beam is essentially treated as beginning to spill off of the sail. This is when the numerical solution switches. Thus,  $\alpha$  can be thought of as a fill threshold. As the projector-to-nanocraft distance increases,  $\alpha$  approaches this threshold until the beam finally falls off. The variable  $b$  meanwhile can be thought of as the fill expansion. It is an exponential term that essentially captures the rapid beam expansion at the start of launch, when acceleration is greatest. The first numerical solution  $\eta_1$  therefore is the beam transfer efficiency when the beam underfills the sail. The second numerical solution  $\eta_2$  therefore is the beam transfer efficiency when the beam overfills the sail.

$$\alpha = \sqrt{\frac{2\pi}{\tau}} \quad (2)$$

$$b = e^{\alpha^2} \quad (3)$$

$$\eta_1 = \frac{1}{4b^2} \left( \alpha^4 + \sqrt{\alpha^8 - 4\alpha^4 b + 4b^2 - 8b + 4} \right)^2 \quad (4)$$

$$\eta_2 = \left( \frac{\alpha^2}{2} - \frac{\alpha^6}{32} + \frac{7\alpha^{10}}{4608} \right)^2 \quad (5)$$

$$\eta_b = \begin{cases} \eta_1, & \alpha > 1.217 \\ \eta_2, & \text{otherwise} \end{cases} \quad (6)$$

Once a value for the transfer efficiency is obtained, it can be used to calculate the amount of power that will map onto the sail from the projector's frame of reference ( $P_b$ ). This quantity is actually dependent upon two transfer efficiencies. The first is the beam transfer efficiency, and the second

is the atmospheric transfer efficiency ( $\eta_a$ ). This value accounts for the power lost due to atmospheric scattering and absorption. It does not, however, take into account the amount of power lost due to atmospheric induced aberrations. This effect is dealt with in the propagation model later on. Mathematically, the atmospheric transfer efficiency is simply a percentage of the total power that will actually exit the atmosphere in a beam that is well-corrected for turbulence and other phase errors. When in conjunction with the beam transfer efficiency and the total power at the projector, the result from Equation 7 is obtained.

$$P_b = \eta_a \eta_b P_1 \quad (7)$$

With an estimate of power on the sail, the kinematic properties of the system can be determined. First, using Equation 8, the relativistic velocity ratio ( $\beta$ ) is found as a fraction of the nanocraft's velocity ( $v_o$ ) to the speed of light ( $c$ ).

$$\beta = \frac{v_o}{c} \quad (8)$$

Equation 9 then uses this ratio, in conjunction with the result from Equation 7, to incorporate the effects of relativity. This results in a value for the power on the sail in the nanocraft's frame of reference ( $P'_s$ ).

$$P'_s = \frac{1 - \beta}{1 + \beta} P_b \quad (9)$$

The force on the sail ( $F_s$ ) is then given by Equation 10. Here, the sail absorptance ( $A$ ) and reflectance ( $R$ ) are incorporated into the model.

$$F_s = \frac{P'_s}{c} (A + 2R) \quad (10)$$

Using the relativistic velocity ratio the Lorentz factor ( $\gamma$ ) is calculated. This value is then used alongside the power on the sail from the projector's frame of reference and sail mass ( $m$ ) to give a final acceleration value scaled by the speed of light ( $\dot{\beta}$ ). This sequence is given by Equations 11-12.

$$\gamma = \frac{1}{\sqrt{1 - \beta^2}} \quad (11)$$

$$\dot{\beta} = \frac{P_b}{\gamma^3 m c^2} \frac{1 - \beta}{1 + \beta} (A + 2R) \quad (12)$$

The final step in the process is to calculate the nanocraft's new kinematic properties. Multiplying the scaled acceleration by the speed of light gives the nanocraft's acceleration ( $a$ ). Classical

mechanics then give the nanocraft's new velocity ( $v$ ) and position ( $z$ ) as a function of the acceleration and time step between calculations ( $dt$ ). These final steps are shown in Equations 13-15.

$$a = \dot{\beta}c \quad (13)$$

$$v = v_0 + a(dt) \quad (14)$$

$$z = z_0 + v(dt) + \frac{1}{2}a(dt)^2 \quad (15)$$

Once these values are determined, they become the new initial conditions and the series of equations is iterated again. The time step is added to the starting time and this process repeats until the final time ( $t_f$ ) is reached. An overview of each of the calculated variables is provided in Table 2.

Table 2. Definitions of calculated variables for kinematic model.

<b>Variable</b>	<b>Definition</b>
$\tau$	Sail fill factor
$\alpha$	Fill threshold
$b$	Fill expansion
$\eta_1$	Underfilled beam transfer efficiency
$\eta_2$	Overfilled beam transfer efficiency
$\eta_b$	Beam transfer efficiency
$P_b$	Power successfully coupled to sail
$\beta$	Relativistic velocity ratio
$P'_s$	Power at sail
$F_s$	Force on sail
$\gamma$	Lorentz factor
$\dot{\beta}$	Acceleration scaled by speed of light
$a$	Nanocraft's new acceleration
$v$	Nanocraft's new velocity
$z$	Nanocraft's new distance from projector

### 3.3 Initial Conditions

The kinematic model was run for a set of initial conditions to satisfy the required propulsion. The conditions chosen were all based on previous and ongoing Starshot research. These parameters are outlined in Table 3. Parkin also used the structure outlined in Section 3.2 to simulate the Starshot system<sup>1</sup>. However, there are several key differences between the initial conditions he used, and the conditions used in this study.

Table 3. Values of initial conditions for kinematic model.

Variable	Definition	Value
$z_o$	Nanocraft's initial distance from projector	$190 \times 10^6$ [m]
$v_o$	Nanocraft's initial velocity	490 [m/s]
$v_f$	Nanocraft's final velocity	$60 \times 10^6$ [m/s]
$a_o$	Nanocraft's initial acceleration	0 [m/s <sup>2</sup> ]
$t_o$	Time at start of launch	0 [s]
$t_f$	Time at end of launch	600 [s]
$dt$	Time step in-between calculations	$10^{-6}$ [s]
$P_1$	Power at projector	$43.617 \times 10^9$ [W]
$D_b$	Projector diameter	4000 [m]
$\lambda_o$	Wavelength of drive light at projector	$1064 \times 10^{-9}$ [m]
$\eta_a$	Loss due to atmospheric scattering and absorption	0.94
$D_s$	Sail diameter	4 [m]
$m$	Nanocraft mass	$10^{-3}$ [kg]
$R$	Sail reflectance	0.999
$A$	Sail absorptance	0.001

Arguably, the most important difference in initial conditions occurs when considering the projector-to-nanocraft starting distance. Parkin uses a value of  $z_o = 6e7$  m while here  $z_o = 1.9e8$  m. The latter value comes from Noyes' research regarding the mothercraft's orbit, while the former comes from a general estimation under the assumption of a low-thrust non-Keplerian orbit. Noyes' value is of particular interest, as it would allow the mothercraft to hang within the projector's isoplanatic patch for the full first 30 s of launch<sup>3</sup>. This is ideal for the guide beacon architecture chosen here and is thus more applicable. Another key difference in initial conditions is the

atmospheric transfer efficiency. Parkin states that this will be a user provided input but does not elaborate on an exact value. The value of  $\eta_a = 0.94$  comes from additional research by Noyes regarding the atmospheric properties above the Atacama Plateau, which will likely be similar in behavior to the actual launch site<sup>9</sup>. Other variations between the initial conditions include the relative values for sail mass and diameter. Parkin assumes a sail mass and diameter of 3.6 g and 4.1 m respectively<sup>1</sup>. However, this study assumes values of 1.0 g and 4.0 m respectively. In general, the rest of the values for the initial conditions are the same for both studies.

An initial nanocraft velocity of  $v_o = 490$  m/s was chosen based on estimates from Noyes using his calculated mothercraft orbit<sup>3</sup>. A time step of  $dt = 1$   $\mu$ s was found to be ideal for smoothing over calculations while minimizing processing time. Upon iterating the model, the power at projector value of  $P_1 = 43.6$  GW was selected. This is the power value found to give the desired propulsion when all other parameters are held constant.

The values for reflectance and absorptance are simply placeholders for future materials. Currently, the material the sail will be constructed of likely does not yet exist. There are separate research groups commissioned to investigate potential candidates. However, the sail will likely have to be reflective as possible to maximize photon drive efficiency. It will also likely have to be absorptive as little as possible to prevent sail destruction. As a result, values of  $R = 0.999$  and  $A = 0.001$  provide a basic starting point. All other initial conditions are the generally agreed upon system parameters, as discussed in Section 1.

### **3.4 Model Results**

Upon iterating the kinematic model with the initial conditions defined in Section 3.3 results were obtained. Figure 6 shows plots illustrating how several of the main kinematic outputs (i.e., acceleration, velocity, and distance) as well as successfully coupled power, force applied to the sail, and the relativistic velocity ratio vary with time. In general, the results behave as anticipated, especially when considering Parkin's previous research.

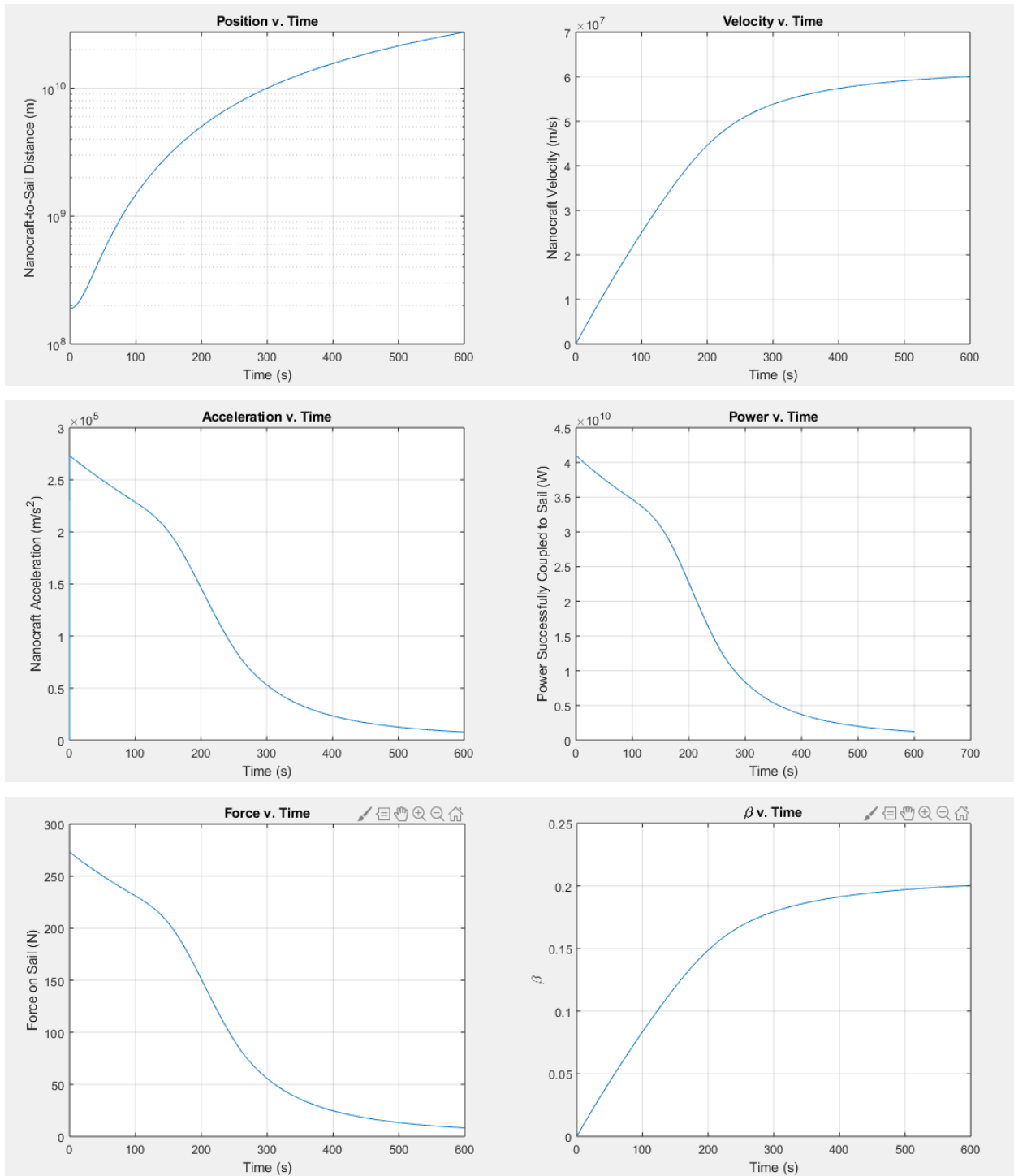


Figure 6. Kinematic model outputs.

The nanocraft reaches a speed of  $6e7$  m/s ( $0.2c$ ) by the conclusion of the launch, as desired. The final projector-to-nanocraft distance is found to be roughly  $z_f = 2.7e10$  m. The distance varies relatively linearly with time after the first 200 s or so, which is expected as the acceleration is initially very large and then decreases over the duration of the launch. The acceleration starts at a

maximum value of  $2.7e5 \text{ m/s}^2$  at the beginning of launch and then drops to a minimum value of  $7.8e3 \text{ m/s}^2$  by the end of launch, following a non-linear pattern that appears to fall within two regimes, as indicated by the “knee” between 100-200 s. This discontinuity ultimately stems from the evolution of the beam transfer efficiency ( $\eta_b$ ) with time. As mentioned in Section 3.2, the analytical solution for this transfer efficiency can be derived from the fact that the beam eventually begins to spill off of the sail as a result of the launch projector’s diffraction limit. This spill-off begins in the 100-200 s window and really starts to become significant at around the 200-300 s mark. While less significant of an effect in magnitude, the redshift of the drive light also leads to a decrease in acceleration. These two effects together reduce the acceleration of the nanocraft which in turn causes the velocity curve to level out as it approaches its maximum value.

Further evidence of this spill-off can be found when considering how beam power coupled to the sail evolves with time. Initially, coupled power decreases only according to relativistic motion, resulting in a linear relationship. Then, between 100-200 s it begins to dip dramatically. This is a direct result of the beam overflowing the sail. The effect becomes increasingly apparent by the end of launch, as only roughly 1.9 GW (4.5% of the total power) maps to the sail. The force on the sail also follows a similar pattern as the acceleration, which follows given the spill-off effect. Initially there is 273.2 N incident upon the sail, but by the end of launch this value is down to 8.3 N. The relativistic velocity ratio behaves as predicted, reaching a value of 0.2 by the end of launch.

### **3.5 Comparisons to Previous Research**

In general, the results of the kinematic model can be qualitatively compared to Parkin’s study, though quantitative comparison is difficult because of the important differences between the initial conditions used in the two cases. The values of many output parameters are not identical to Parkin’s, though they are similar in trend. Comparable plots for velocity and power are not given by Parkin, but acceleration, distance, force, and  $\beta$  are all provided. It is worth noting that in both of Parkin’s acceleration and force plots the trends are similar to those shown in Figure 6 proceeding the 5 minute mark, but prior to that both quantities are relatively constant. This is due to the fact that Parkin assumes the launch aperture power will initially be throttled back to prevent the sail from overheating, and in turn, power dependent quantities are constant for the first portion of the

launch<sup>1</sup>. It is worth noting this is due to assumptions about the properties of the sail material which have not yet been established by the Starshot project.

## **4. PROPAGATION MODEL**

### **4.1 Previous Research and Modeling**

While previous studies have revolved around modeling the system kinematics, outside the scope of this study there is little to no prior research on the system's radiometric response. This is not a regime Parkin explored in detail. The study presented here is the first known to explore this aspect of the project, and the finalized version uses the propagation model to do this. Work on the model started with a foundation that is no longer in use.

When construction of the model began for this study, the propagation model was initially built in FRED, an optical modeling software widely used for non-sequential ray-tracing. The model's preliminary design is outlined by Rice in "Preliminary Model for Radiometric Design and Analysis of the Breakthrough Starshot Initiative"<sup>4</sup>. In Rice's paper the FRED model was stated to be the starting point for future research. However, since discovering some disadvantages of the FRED approach, the propagation model has pivoted to a new structure. Some of the preliminary irradiance profiles generated using this model are shown in Figure 7. The beams modeled here are of ideal Gaussian profile in nature. Atmospheric effects (i.e. absorption, scattering, turbulence) are not considered.

While FRED seemed ideal for this type of modeling at first, it was found to be impractical due to the system's extreme length. In order to accurately model the drive light using rays, Gaussian beam decomposition (GBD) would have to be used. The algorithm FRED uses for this is highly effective when modeling typical optical systems, but is not meant for use over distances on the order of millions of kilometers. The Gaussian beam would have to be resampled many times to avoid diverging too far. Without resampling, the beam was demonstrating behavior, particularly when summing up total power at the sail, that was known to be inaccurate. Attempts were made at effectively sampling the beam, but the exact architecture for this was never fully identified. As a result the model was built in MATLAB instead.

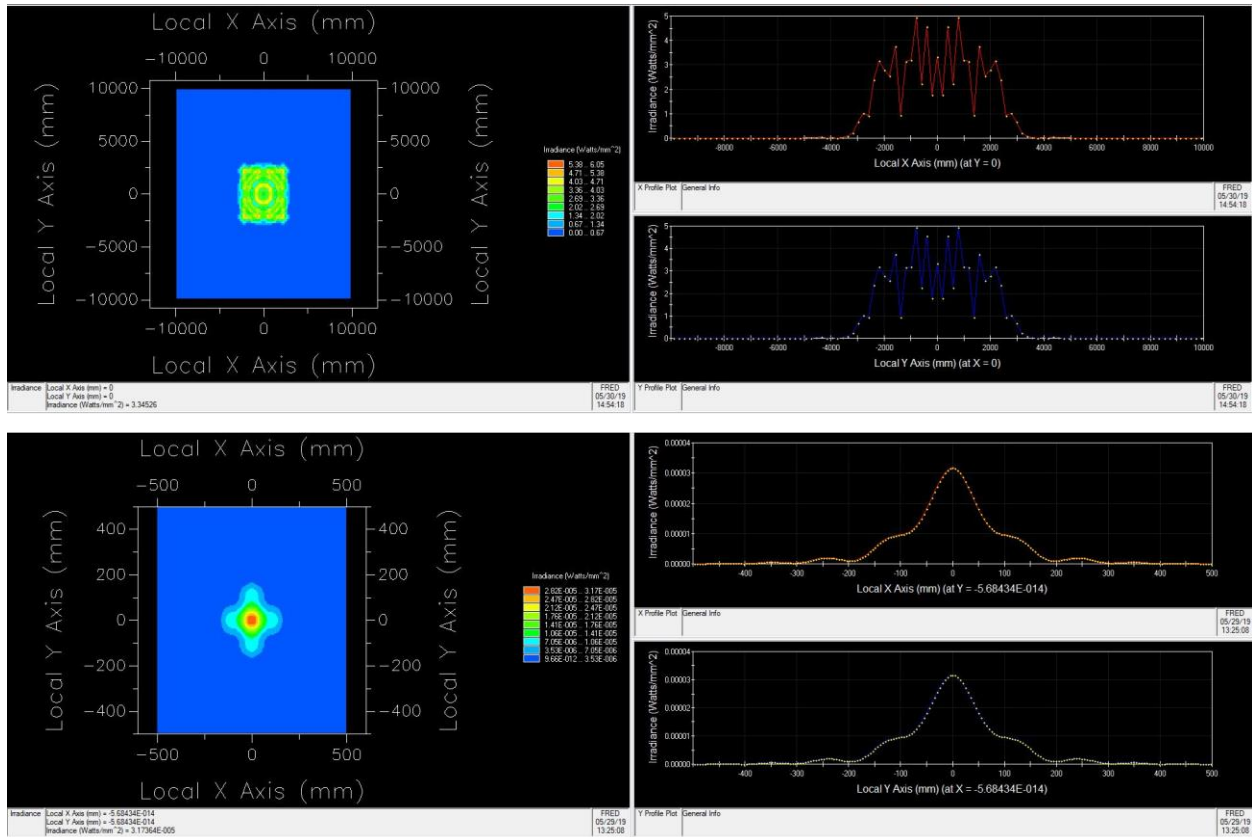


Figure 7. Preliminary irradiance profiles generated in FRED<sup>4</sup>.

## 4.2 Model Structure

The propagation model characterizes the drive light at multiple locations in the Starshot system over the launch duration. The model is constructed so that values can be provided at any point in time larger than the chosen time-step ( $dt$ ) used in the kinematic model. The model is built in MATLAB and works using Fourier propagation. Thus, the assumption is made that the light is always focused on the sail, according to the launch projector's diffraction limit. This allows for calculations of power and irradiance at the sail without implementing ray-tracing. In the real system this may be problematic from a sail perspective, as focusing all of the power on the sail, particularly at the start of launch when the beam footprint is very small, could punch a hole in the sail. Purposely defocusing the beam in the early stages of launch may help mitigate this effect. However, even if the beam were defocused, the defocus would likely be just enough to fill the sail and all power would still be incident. As a result, for the purposes of studying radiometric response, the assumption works well. The basic geometrical layout of the system is displayed in Figure 8.

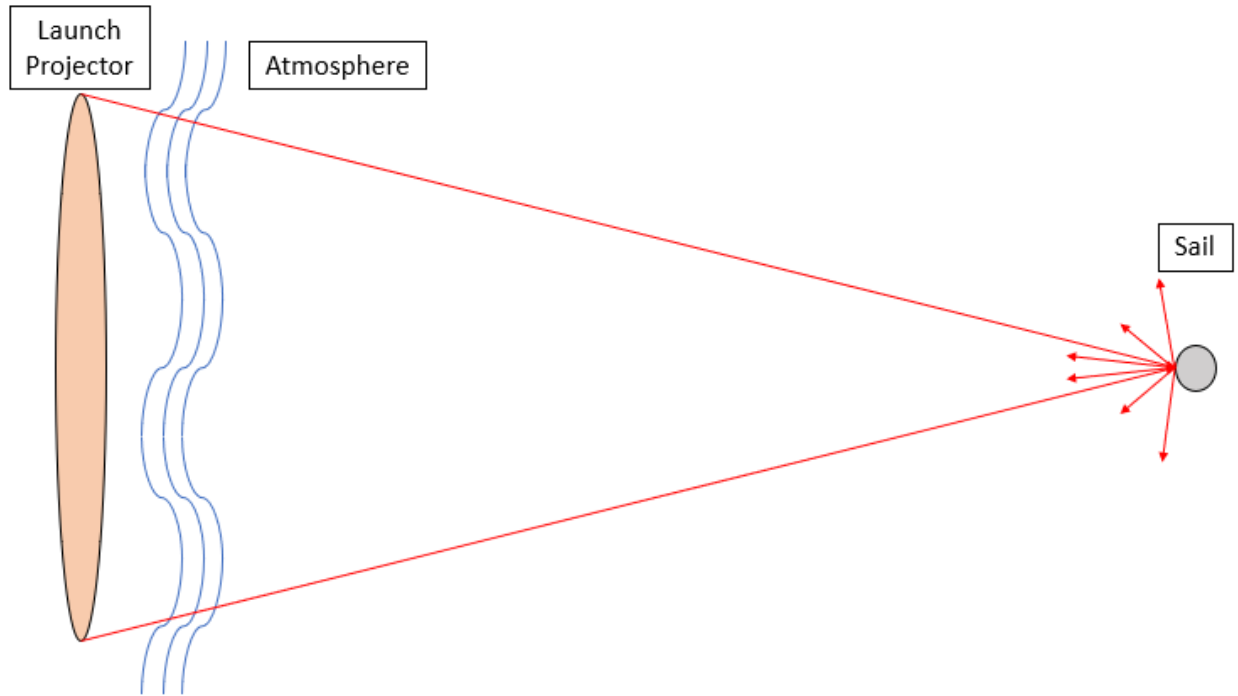


Figure 8. Basic geometric layout of system propagation.

In general, the model propagates the initial projector beam from the launch projector aperture, through the atmosphere, and to the sail. Once at the sail, the beam is reflected, in accordance with a chosen BRDF. The drive light power is summed up before and after reflection, and corresponding irradiance maps are produced. In particular, only the light reflected back into the solid angle of the projector is considered, as this is the light viable for use in wave-front sensing. The model performs this sequence using several sections that each play important roles in accurately simulating propagation.

The first section of the model sets the initial conditions. All initial conditions are identical to those provided in the kinematic model, so as to maintain consistency with the outputs provided from the kinematic results. The only additional initial conditions are projector-to-nanocraft distance at the end of launch ( $z_f$ ), and the sail pixel resolution ( $D_{\text{pix}}$ ). The first of these values simply defines the range over which propagation takes place, while the second essentially designates the number of pixels across the sail. This can be likened to setting the number of individual rays in a ray-tracing software such as CODE V or Zemax. All initial conditions are given in Table 4.

Table 4. Values of initial conditions for propagation model.

Variable	Value
$z_o$	$190 \times 10^6$ [m]
$z_f$	$2.741 \times 10^{10}$ [m]
$P_l$	$43.617 \times 10^9$ [W]
$D_b$	4000 [m]
$\lambda_o$	$1064 \times 10^{-9}$ [m]
$\eta_a$	0.94
$D_s$	4 [m]
$D_{pix}$	1000 [pix]

Once the input conditions are established the next section of the model creates the sail. For the purposes of this study, only a spherical sail was used. The sail's spatial geometry, in pixels, was generated using Equation 16.

$$Sail(x, y) = \sqrt{\left(\frac{D_{pix}}{2}\right)^2 - \left(\frac{y - D_{pix}}{2}\right)^2 - \left(\frac{x - D_{pix}}{2}\right)^2} \quad (16)$$

A circular mask the diameter of the sail is then applied over the sail to ensure that only rays contacting the sail are reflected. The sail is shown in Figure 9. The color bar in in units of pixels.

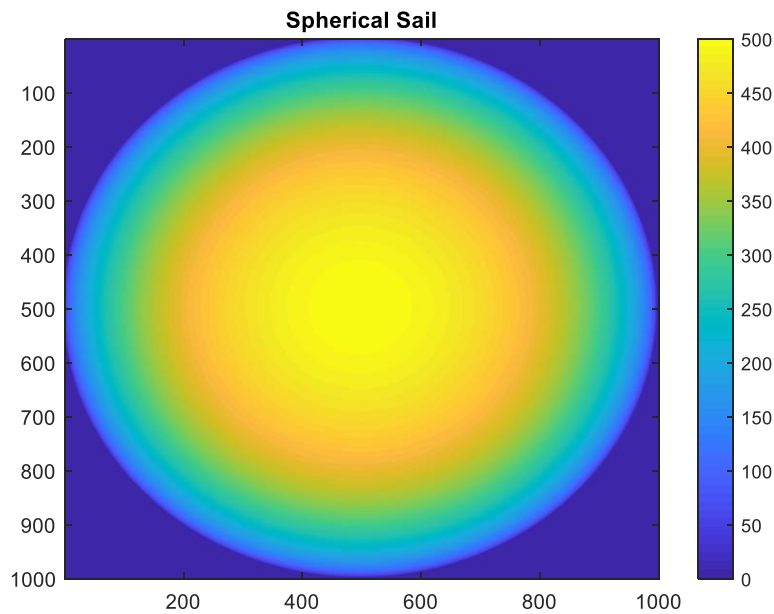


Figure 9. Sail in propagation model.

Upon creation of the sail, the next section calculates the angle ( $\theta_{ray}$ ) between each incoming ray ( $\vec{i}$ ) and the surface normal ( $\vec{n}$ ) of the pixel it contacts. This will be useful later on when calculating the amount of light reflected back towards the projector. The key assumption made here is that all incoming rays are virtually parallel with the normal of the center of the sail. Given the vast distances and extremely small angles involved in propagation, this assumption appears reasonable. Thus, each ray is defined as travelling only in the z-direction, where the z-axis is the system's optical axis, by the time the beam contacts the sail. At this point, the surface normals of each pixel are generated using MATLAB's "surfnorm" function, and Equation 17 is used to calculate the angle. The reflection geometry is shown in Figure 10 for an off-axis sail pixel<sup>5</sup>. One can think of this as a portion of the sphere whose normal is removed by some angle ( $\theta$ ) from the optical axis (i.e. side of the sphere when viewed head on from the projector). Each sail pixel is represented by an area element ( $dA$ ) while  $\theta_{ray} = \theta$ . The reflected ray is represented by ( $\vec{r}$ ).

$$\theta_{ray} = \cos^{-1} \left( \frac{\vec{i} \cdot \vec{n}}{\|\vec{i}\| \|\vec{n}\|} \right) \quad (17)$$

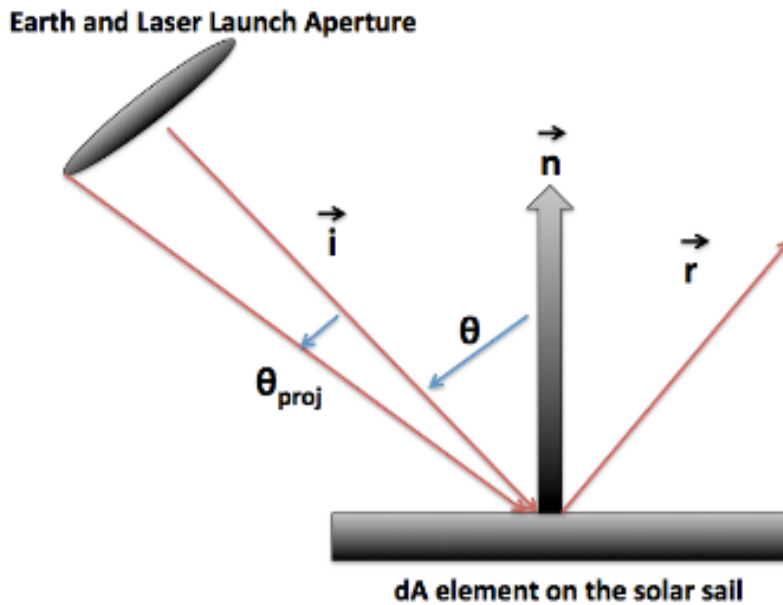


Figure 10. Geometry of sail reflection. The  $dA$  area element is off-axis with the incoming beam on-axis<sup>5</sup>.

The next section of the model is the final portion, and this is where the actual propagation takes place. This section includes phase generation, atmospheric simulation and AO correction, amplitude generation, Fourier propagation, and finally reflection off of the sail using BRDF integration. This study focuses on examining the system's radiometric response given three different types of beam PSF (i.e. Gaussian, donut, and four-lobed) for the purposes of considering

sail stability. Therefore, the section comes in three flavors, but all three follow the same general format.

To start, a general array size ( $D_{array}$ ) for any plane in the path of propagation is defined. This is not the size of the sail, but rather significantly larger. For all figures in this section the array size is  $D_{array} = 10000$  pixels. The assumption is that nearly all of the drive light will be collected by this plane. This is ideal for scaling power at the sail plane after the Fourier transform is applied. The larger the array size, the more accurate the measurement as the sampling increases. However, large array sizes also strain MATLAB storage capacity. An array size of 10000 pixels was found to be optimal for most PSFs when considering both factors.

With the array size defined, a scaling factor (SF) for the launch aperture diameter ( $D_{aper}$ ) is calculated. The scaling factor varies the launch aperture diameter as a function of projector-to-nanocraft distance so that the beam diameter on the sail is always equal to the launch projector's diffraction limited spot size ( $D_{diff}$ ), as specified according to Equation 18.

$$D_{diff}(z) = 2z \tan\left(\frac{1.22\lambda_o}{2D_b}\right) \quad (18)$$

As the aperture size gets smaller, the beam footprint in the plane of the sail gets larger. While the actual launch aperture will not change in size, this works well for the purposes of simulation. It has the same effect as using a constant launch aperture diameter at every point in the launch and changing the sail size. The change in angular subtense is accounted for in both scenarios, and scaling the launch aperture size is advantageous when compared to scaling the sail size for minimizing MATLAB storage memory. Both the scaling factor, and resulting aperture size, are given by Equations 19-20.

$$SF(D_{diff}) = \frac{D_{pix}D_{diff}}{2D_s} \quad (19)$$

$$D_{aper}(SF) = \frac{D_{array}}{SF} \quad (20)$$

With the scaling in place, beam generation can begin. First, the ideal phase ( $\phi_{ideal}$ ) corresponding to the desired PSF is generated across the aperture size. The various PSF phases are described in Section 5.2. Following this process, the atmosphere can be considered. Atmospheric turbulence is added to the ideal phase through the process of calling on several functions. The first of these

functions generates raw turbulence in the form of von Karman phase screens. Von Karman phase is used as opposed to Kolmogorov phase because of the extreme launch projector diameter<sup>10</sup>. The diameter is so large that the outer scale ( $L_o$ ) must be taken into account. The outer scale for this study was chosen to be  $L_o = 80$  m, based on a series of measurements taken by Takato et al.<sup>11</sup>. The function follows the behavior of the von Karman power spectrum ( $\Phi$ ) outlined in Equations 21-23. Normally, the von Karman power spectrum would be scaled using a  $C_n^2$  profile. However, this scaling is taken care of after turbulence generation using an amount of allowable residual wavefront error, as explained later on in this section.

$$\Phi(\kappa) = (\kappa^2 + \kappa_o^2)^{-\frac{11}{6}} \quad (21)$$

$$\kappa = x^2 + y^2 \quad (22)$$

$$\kappa_o = \frac{2\pi D_b}{L_o D_{aper}} \quad (23)$$

Phase is generated in accordance with the method given by Lane et al., which adds in under-sampled low-frequency components<sup>12</sup>. This prevents a lack of low-frequency power and results in more accurately sampled phase screens than those given by other methods. A new phase screen is generated for each projector-to-nanocraft distance. The assumption is that the atmospheric coherence time ( $\tau_o$ ) is smaller than the time taken for the nanocraft to reach each new position where measurements are made. While this would not necessarily always be true, as a result of processing time only a small sample of projector-to-nanocraft distances are considered for each system configuration. Thus, the time in between measurements is on the order of minutes, which is significantly larger than  $\tau_o$  (likely to be on the order of a few milliseconds at  $\lambda = 1064$  nm).

Importantly, the phase screens are each generated across the appropriate aperture diameter corresponding to the projector-to-nanocraft distance in question. This ensures that the same amount of residual phase is achieved at every projector-to-nanocraft distance. One can think of this as scaling the beam's atmospheric footprint. As the aperture size scales to achieve the appropriate diffraction limited spot size, so does the portion of atmosphere the beam propagates through. In Figure 11, a sample von Karman phase screen has been generated for the aperture size corresponding to the initial projector-to-nanocraft distance of  $z = 1.9e8$  m. The color bar is in units of radians.

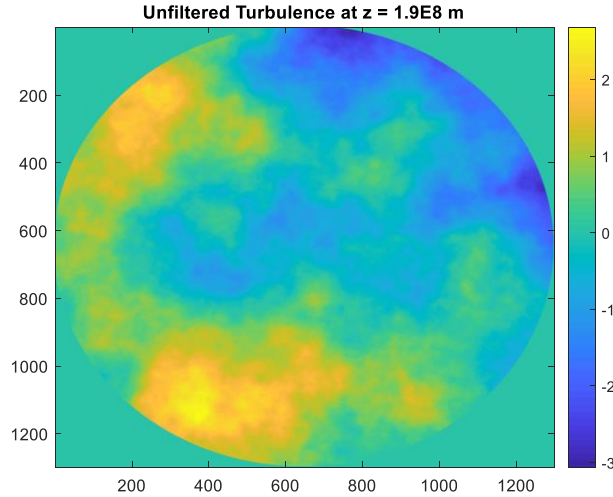


Figure 11. Unfiltered von Karman turbulence.

With the phase screen generated, a simulated AO correction is applied to give a final residual phase error ( $\varphi_{\text{residual}}$ ) that can be added to the ideal beam phase. This correction is performed using a filtering function that generates Zernike polynomials and checks to see how much each term contributes to the overall phase error. The first 20 Zernike terms are used, as this was found to be the best amount for optimizing processing speed while still achieving quality correction. After determining the individual contributions, the terms are removed accordingly. The resulting residual is then scaled by an allowable amount of wave-front variance of each correction ( $\sigma_{\text{corr}}^2$ ). Because each phase screen is created using an aperture size corresponding to a specific projector-to-nanocraft distance, this correction is always applied across what is essentially the beam's full footprint in the atmosphere, giving equal amounts of residual phase at all projector-to-nanocraft distances. The allowable wave-front variance stems from the user's choice in total power at the launch aperture.

According to the results from the kinematic model, the amount of required incident power on the sail at the starting projector-to-nanocraft distance to achieve the desired propulsion is  $P_b = 41$  GW. Taking into account the atmospheric transfer efficiency of  $\eta_a = 0.94$ , this implies that ideally there must be a total power at the launch aperture of roughly  $P_1 = 43.6$  GW in a diffraction limited beam. This value is fixed for every system configuration considered in the propagation model. However, in the real system the beam will quickly be aberrated by the atmosphere and no longer diffraction limited. Thus, a power greater than the  $P_1$  value given by the kinematic model will be required, and

the amount of extra power required will be set by the quality of the AO correction. Essentially, a trade-off is presented. The initial projector beam can be of much higher power than needed in the ideal circumstance, and the requirements on AO performance are less strict. Conversely, the beam can be corrected very well, and less extra power is required. To facilitate studying this trade-off, the parameter allowed to vary is the actual power at the projector ( $P_{real}$ ). This value is then used alongside the  $P_1$  value given by the kinematic model in the Strehl ratio ( $S$ ) formula provided by Equation 24.

$$S(P_{real}) = \frac{\eta_a P_l}{\eta_a P_{real}} \quad (24)$$

The Strehl ratio calculated is then used via the Marechal approximation in Equation 25 to specify an amount of allowable wave-front variance in each correction. This variance sets the limits on how well the AO correction simulation can operate.

$$\sigma_{corr}^2(S) = -\ln(S) \quad (25)$$

The plot in Figure 12 exhibits the same von Karman phase screen as in Figure 11, except with correction corresponding to a Strehl of 50%. The color bar is in units of radians. After this process, the aperture is placed within the larger general array size to be compatible with the ideal phase.

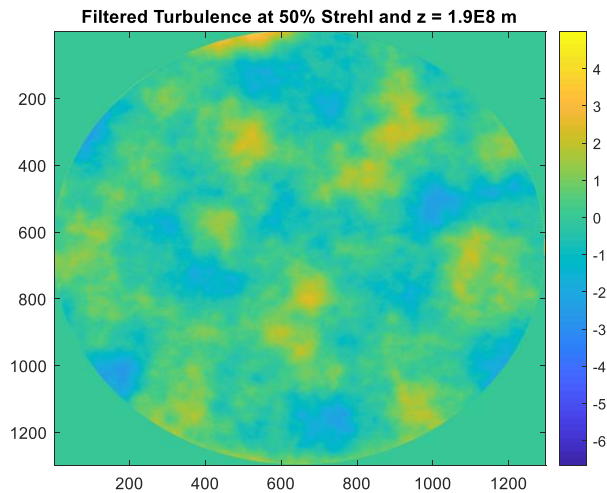


Figure 12. Filtered von Karman turbulence.

Furthermore, an average of two perpendicular cross sections through the power spectrum before and after filtering is provided in Figure 13. As shown, the spectrum has an absence of lower frequency data post filtering, exhibiting an effect similar to that of a high-pass filter. This is expected with the removal of the lower-order Zernike terms performed by the filtering function.

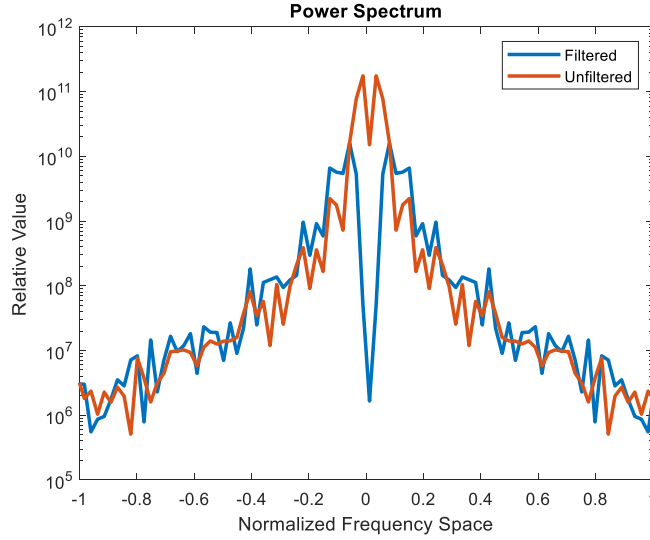


Figure 13. Unfiltered and filtered power spectrum.

Now that the desired atmospheric turbulence, post AO correction, has been obtained, the phase residual is added to the initial beam's phase in Equation 26.

$$\varphi = \varphi_{ideal} + \varphi_{residual} \quad (26)$$

Following phase generation, field amplitude ( $A$ ) is calculated using a circular aperture mask. This circular aperture mask is scaled according to the corresponding aperture size and varies for each PSF shape. Each beam's amplitude is outlined in Section 5.2. At this point the phase and amplitude are both across the correct aperture size for any given projector-to-nanocraft distance, but centered upon the larger array size. As mentioned previously, this creates a beam diameter on the sail equal to the launch projector's diffraction limited spot size ( $D_{diff}$ ). This results in a beam that eventually spills off of the sail. The amplitude and phase are used in Equation 27 to give the field ( $E$ ).

$$E = Ae^{-i\varphi} \quad (27)$$

This field is then Fourier propagated and squared to produce irradiance ( $I_{total}$ ) over the full array size at the plane of the sail using Equation 28.

$$I_{total} = |F_2\{E\}|^2 \quad (28)$$

At this point, everything is in terms of the larger array size specified at the beginning of propagation. However, as previously stated this is significantly larger than the actual sail size. Therefore, the irradiance must be cropped to the sail dimensions (i.e.  $D_{pix} = 1000$ ). Prior to cropping, the power is scaled to the known value of  $P_b = 41$  GW given by the kinematic model.

The full irradiance is now cropped using Equation 29 and the resulting irradiance ( $I_{sail}$ ) is treated as the amount of light that makes it to the 4 m diameter sail.

$$I_{sail}(x, y) = \begin{cases} I_{total}(x, y), & \left(x - \frac{D_{array}}{2}\right)^2 + \left(y - \frac{D_{array}}{2}\right)^2 \leq \left(\frac{D_{pix}}{2}\right)^2 \\ 0, & otherwise \end{cases} \quad (29)$$

Using Equation 30, the individual power contributions from each pixel can be summed up to give a total power incident on the sail ( $P_{sail}$ ).

$$P_{sail} = \sum_{x,y} I_{sail}(x, y) \quad (30)$$

Sample irradiance profiles incident upon the sail for a donut PSF are displayed in Figure 14. The color bar is in units of Watts for both plots. It is worth noting that the donut has a floor set to roughly 20% of its peak value. The profiles correspond to the initial projector-to-nanocraft distance of  $1.9 \times 10^8$  m and about a quarter of the way through launch at  $z = 7 \times 10^9$  m. The Strehl ratio is 50%, as it was in the filtered turbulence. The profile on the left has been zoomed in on so that features can be seen. This is because the footprint is much smaller than the sail at the initial projector-to-nanocraft distance, which is expected. Additionally, the profile on the right has actually begun to spill off of the sail, which can clearly be seen as the outer-most circular aperture in the profile.

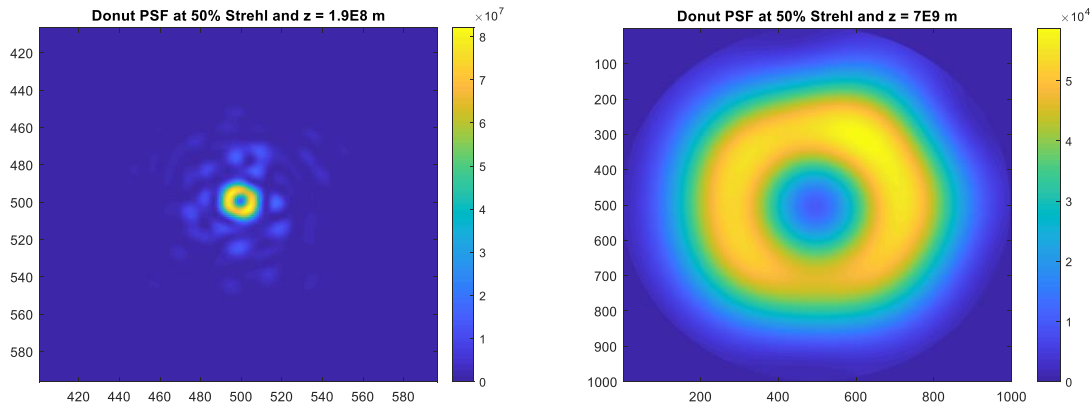


Figure 14. Incident PSF profiles on sail.

The two patterns are not identical in appearance, but this is because of the way the turbulence function generates phase screens. The function uses an array of randomly generated numbers, the size of which corresponds to a given aperture size. Therefore, a new array, and consequentially phase screen, is always generated at each new projector-to-nanocraft distance. This ensures that the atmospheric footprint is scaled, as mentioned previously. Accordingly, regardless of aperture diameter the same amount of residual will be generated upon AO filtering as a result of the user

specified allowable wave-front variance. Regardless, the patterns do not need to be identical since all measurements in this study are taken between times greater than  $\tau_o$ .

Now that the irradiance at the sail has been obtained, the sail reflection is simulated. In order to properly do this, a BRDF must be defined. This study only considers one BRDF since the drive space parameters are held constant. The BRDF is defined in Section 5.1, but can be considered specular for the purposes of this section. The only reflected drive light of consideration is that which reflects back into the angle subtended by the projector ( $\theta_{proj}$ ), as defined by Equation 31.

$$\theta_{proj}(z) = 2 \tan^{-1} \left( \frac{D_{proj}}{2z} \right) \quad (31)$$

As a result, the BRDF is integrated over this angle. Using Equation 32, an irradiance contribution, per pixel, back towards the projector is calculated ( $I_{back}$ ). The angle defining the cone of reflection ( $\phi$ ) serves as essentially the solid angle multiplier. This angle is always integrated over  $2\pi$  to give a full rotation about the reflected ray. Thus, the BRDF, which is given in units of  $\text{sr}^{-1}$ , is multiplied by  $2\pi \text{ sr}^{-1}$  and the units cancel out.

$$I_{back}(\theta, \phi) = \int_0^{2\pi} \int_{\theta_1}^{\theta_2} BRDF(\theta) I_{sail}(x, y) d\phi d\theta \quad (32)$$

The bounds of the integral ( $\theta_1$  and  $\theta_2$ ) are given by Equations 33-34, where again  $\theta_{ray}$  is the angle between the surface normal at each sail pixel and the incoming drive light.

$$\theta_1(x, y) = 2\theta_{ray}(x, y) \quad (33)$$

$$\theta_2(x, y) = 2\theta_{ray}(x, y) + \theta_{proj} \quad (34)$$

Then, similarly to the case with the power incident upon the sail, the power reflected back towards the launch projector ( $P_{back}$ ) is found using Equation 35.

$$P_{back} = \sum_{x,y} I_{back}(x, y) \quad (35)$$

This is the final step in the propagation model, as the power both incident upon the sail, as well as reflected back towards the launch projector, has been characterized and quantified. Figure 15 gives irradiance profiles reflected back towards the projector corresponding to the incident profiles in Figure 14. Once again, the plot on the left has been zoomed in one while the plot on the right has not. The color bar is in units of Watts for both plots.

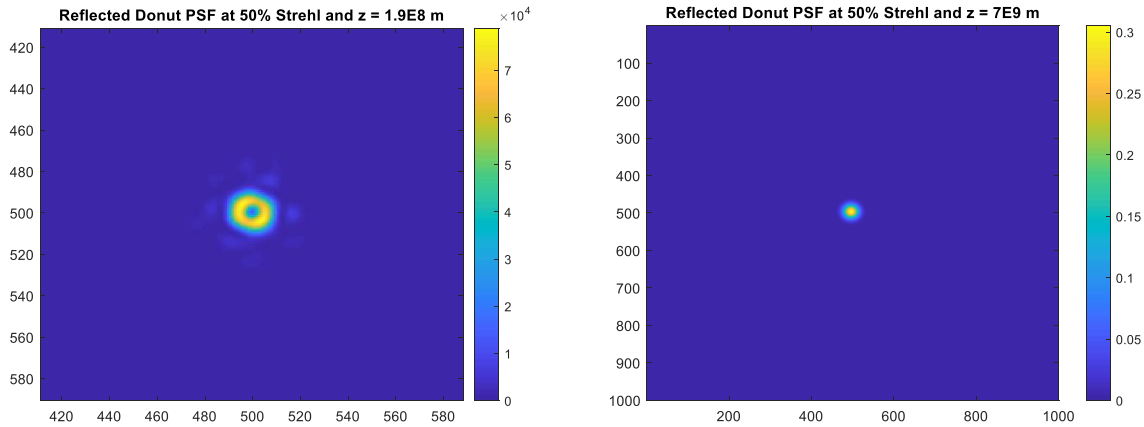


Figure 15. Reflected PSF profiles back towards projector.

The two profiles exhibit interesting, but not unexpected, behavior. At the initial projector-to-nanocraft distance the beam is smallest and interacts with just the very center of the sail. In this regime, the sphere is closest to a flat mirror, and given the fact that the BRDF is relatively specular, the majority of the donut reflects back towards the projector, resulting in a similar shaped irradiance profile of slightly lesser magnitude. It is worth noting again that the beam is likely to be defocused in this regime in the actual system, and will always provide more return light at the initial projector-to-nanocraft distance than at others. However, at the next distance the incident irradiance is roughly the size of the sail, as shown in Figure 13. As a result, only the central floor component reflects back towards the projector while the outer ring of the donut contacts the sail at much higher angles of incident and reflects specularly away.

The results of this model have been verified by Bowers using a Gaussian beam incident upon a flat Lambertian sail<sup>5</sup>. In his study, Bowers calculates the theoretical amount of return light given these parameters using basic radiometric equations. He finds that in an ideal scenario (i.e. no atmospheric turbulence) the model and theoretical estimations each predict return powers within about 6% of each other. The difference in magnitude of about 0.06 can be explained by slight discrepancies between Bowers' theoretical assumptions regarding beam fall-off, and the model's calculations. However, in general these results are obviously very similar in nature and support the assumption that the model is simulating the beam's evolution with time relatively accurately.

With this architecture in place, the model can now be used to conduct a trade study that examines multiple beam shapes, as well as variations in the overall starting power and AO performance.

## 5. TRADE STUDY PARAMETERS

### 5.1 Constant Drive Space Parameters

The drive space parameters are all held constant for the purposes of this study, as only launch space parameters are allowed to vary. The main parameters considered here are the sail shape and BRDF profile. The values for both of these parameters were chosen based on recent estimates from other Starshot research efforts, so as to accurately depict the potential system.

The sail shape was chosen to be spherical, as depicted in Figure 9 and Equation 16. There is no set sail shape, but from a stability standpoint spherical profiles have advantages. In Hyatt's work, sail stability is explored<sup>6</sup>. It is found that more than likely, it will be difficult to drive a flat or semi-flat sail. One can liken the situation to a piece of paper balancing on a pencil. If the pencil is decentered by even a small amount, the paper will fall off in the opposite direction. In this case the sail will not only have to balance in the beam, but it is going to undergo extreme force pushing it away from the projector. Additionally, there will be no closed-loop control for the stability, as the round-trip time-of-flight is too long. If the beam is off-center, the sail is almost sure to go flying off course in fractions of seconds. However, this may not necessarily be the case if the sail is spherical.

Given the right PSF shape, such as a donut, a spherical sail may actually self-correct this decentering to a degree<sup>6</sup>. It will balance inside the donut, much like a ball on a ring. If the PSF is off-center, the sail will naturally feel a restoring force pushing it back towards the center of the PSF. This will work unless the PSF is so far off-center that it imparts a force great enough to push the sail over the donut peak and resultingly off course. While not perfect, this proposition has promise and helps address some of the pressing issues in the project's early phases. There may be other sail shapes that will be considered in the near future but given present studies the spherical shape is one of the most relevant. Therefore, it was selected for the simulations presented here.

The BRDF profile was selected based on approximations for potential sail materials made by Bowers<sup>5</sup>. A material prevalently used in modern spacecraft is known as Kapton polyimide. Kapton is similar to Mylar, another common spacecraft material, and features high mechanical durability as well as resistance to space-based radiation. Both of these qualities make it a reasonable starting point for a sail material. In the work outlined by Reyes et al. the optical properties of Kapton are

characterized<sup>13</sup>. In particular, measured BRDF profiles are provided. Figure 16 shows the BRDF of Kapton, with the 0° line being the function of interest.

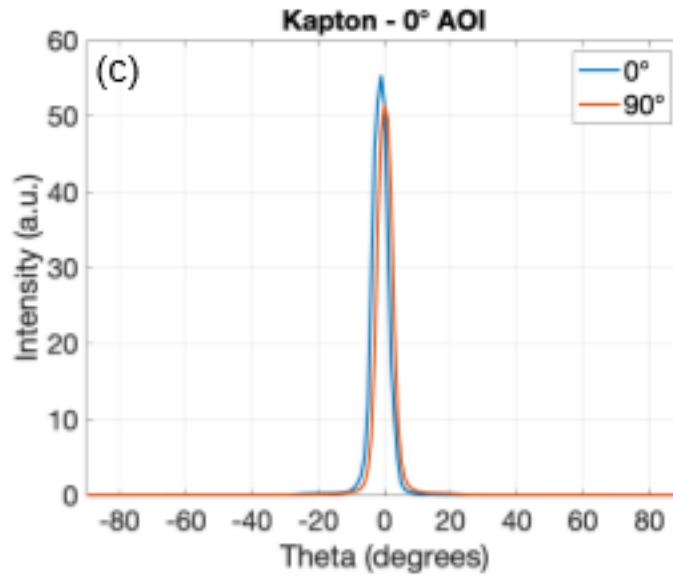


Figure 16. BRDF of Kapton polyimide<sup>13</sup>.

The data was imported into MATLAB and a “gauss2” fit was applied to give a reasonable approximation to the figure above. This provided the BRDF given by Equation 36.

$$BRDF(\theta) = 61.58 * e^{-\left(\frac{\theta+4.992*10^{-5}}{3.979}\right)^2} + 0.745 * e^{-\left(\frac{\theta-17.25}{4.972}\right)^2} \quad (36)$$

This BRDF value is plugged into Equation 32 and used for the entirety of this study.

## 5.2 Varied Launch Space Parameters

The launch space parameter of interest is the projector beam PSF. Three PSF shapes are used in this trade study: Gaussian, donut, and four-lobed. Each of the three has been chosen because of relevance to current Starshot research.

The Gaussian PSF is used as it is a reasonable baseline for most laser beams. While the actual beam may vary from the traditional Gaussian shape, it provides a benchmark to compare results to. In the propagation model, the beam’s ideal phase is generated simply as an array of zeros with a diameter equal to that of the chosen array size. The beam amplitude is given by Equations 37-40 as a simple Gaussian modulated by a circular mask with a diameter corresponding to the aperture

size used to generate a diffraction limited spot size at the sail for each projector-to-nanocraft distance, as explained in Section 4.2.

$$A(x, y) = \begin{cases} \frac{1}{\rho\sqrt{2\pi}} e^{-\left(\frac{(x-x_0)^2}{(2\rho)^2} + \frac{(y-y_0)^2}{(2\rho)^2}\right)}, & \left(x - \frac{D_{array}}{2}\right)^2 + \left(y - \frac{D_{array}}{2}\right)^2 \leq \left(\frac{D_{aper}}{2}\right)^2 \\ 0, & otherwise \end{cases} \quad (37)$$

$$\rho = 0.15D_{array} \quad (38)$$

$$x_0 = \frac{D_{array}}{2} \quad (39)$$

$$y_0 = \frac{D_{array}}{2} \quad (40)$$

The basic Gaussian PSF shape is shown on the sail at the initial projector-to-nanocraft distance of  $z = 1.9e8$  m in Figure 17. The beam is truly a Gaussian convolved with an airy disk due to the circular aperture. The PSF is zoomed in on, as it is small at the initial projector-to-nanocraft launch distance. This figure is produced in the ideal scenario where there is no atmospheric turbulence. In the full simulations this is not the case as turbulence is added to the ideal phase. The color bar is in units of Watts.

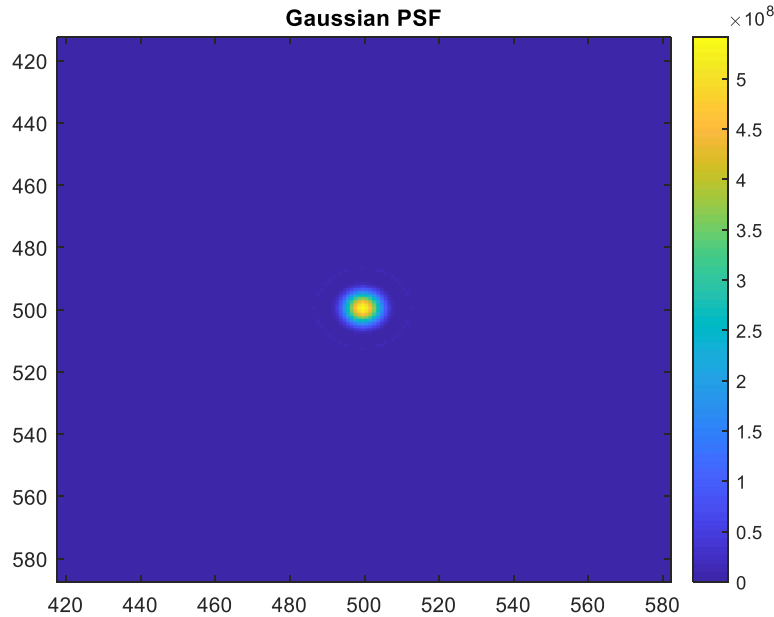


Figure 17. Diffraction limited Gaussian PSF at start of launch.

The donut PSF is used for similar reasons to those concerning the spherical sail explored in Section 5.1. For a spherical sail, a donut PSF provides a potential answer to the problem of achieving sail

stability<sup>6</sup>. The donut PSF used here is actually modified slightly to have a floor, making it more of a bowl shape. This floor is set to roughly 20% of the donut peak and serves as an additional stabilizing feature. The force differential applied by a true donut (i.e. zero power in the center) across the sail may be enough to tear the sail apart. By adding some power to the center, this differential is decreased. It is worth noting that the higher the floor gets, the greater risk the sail has of falling out of the beam. Therefore, there is a trade-off here and this is something researchers are examining. The beam's ideal phase is generated as a vortex phase, given by Equation 41.

$$\varphi_{ideal}(x, y) = \left\{ \begin{array}{ll} \tan^{-1} \left( \frac{x - \frac{D_{array}}{2}}{y - \frac{D_{array}}{2}} \right) + \frac{\pi}{2}, & y - \frac{D_{array}}{2} > 0 \\ \varphi_{ideal}(x, y) + \pi, & otherwise \end{array} \right\} \quad (41)$$

The beam amplitude is simply set to a value of A=1 when modulated by the same circular mask as used for the Gaussian. This is given by Equation 42.

$$A(x, y) = \left\{ \begin{array}{ll} 1, & \left( x - \frac{D_{array}}{2} \right)^2 + \left( y - \frac{D_{array}}{2} \right)^2 \leq \left( \frac{D_{aper}}{2} \right)^2 \\ 0, & otherwise \end{array} \right\} \quad (42)$$

In Figure 18 the donut PSF is shown. One again, this is for the case of the initial projector-to-nanocraft distance of  $z = 1.9e8$  m and no atmospheric turbulence. The color bar is in units of Watts.

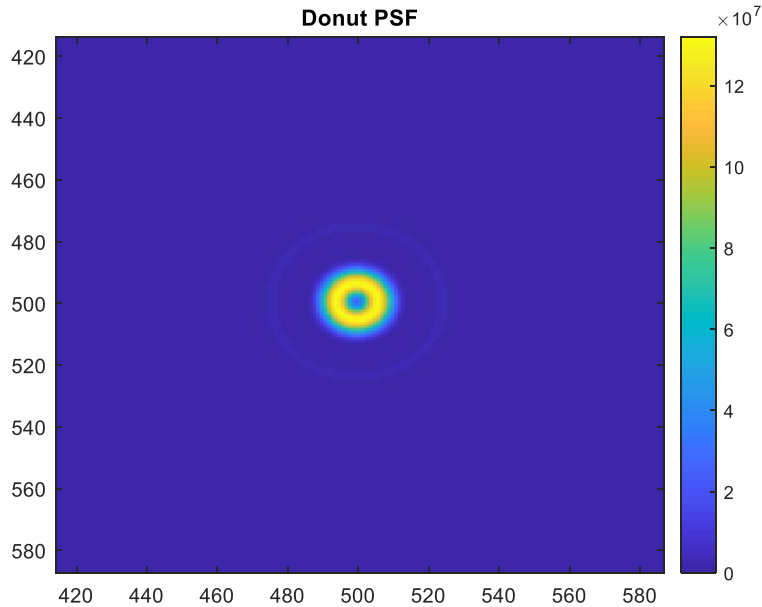


Figure 18. Diffraction limited donut PSF at start of launch.

The four-lobed PSF is also considered for stability purposes. As shown by Hyatt, the four-lobed approach gives a similar effect to that of the donut, as the sail can ride in the middle of the four quadrants<sup>6</sup>. There are multiple proposed methods of generating the beam including four separate Gaussians as well as applying quadrant phase. There have also been discussions of phase shifting the beam in time to generate quick pulses in each of the four quadrants. From an engineering standpoint, the quadrant phase may be more convenient to implement than four separate Gaussians, and thus is the approach used here. The quadrant phase is given by Equation 43.

$$\varphi_{ideal}(x,y) = \begin{cases} \frac{\pi}{2}, & x - \frac{D_{array}}{2} < 0 \ \& \ y - \frac{D_{array}}{2} > 0 \\ \pi, & x - \frac{D_{array}}{2} < 0 \ \& \ y - \frac{D_{array}}{2} < 0 \\ \frac{3\pi}{2}, & x - \frac{D_{array}}{2} > 0 \ \& \ y - \frac{D_{array}}{2} < 0 \\ 2\pi, & x - \frac{D_{array}}{2} > 0 \ \& \ y - \frac{D_{array}}{2} > 0 \end{cases} \quad (43)$$

Just as in the case of the donut, the beam amplitude is simply set to a value of A=1 when modulated by the same circular mask as used for the Gaussian. This is once again given by Equation 42. The four-lobed PSF is shown in Figure 19 for the case of the initial projector-to-nanocraft distance of  $z = 1.9e8$  m and no atmospheric turbulence. The color bar is in units of Watts.

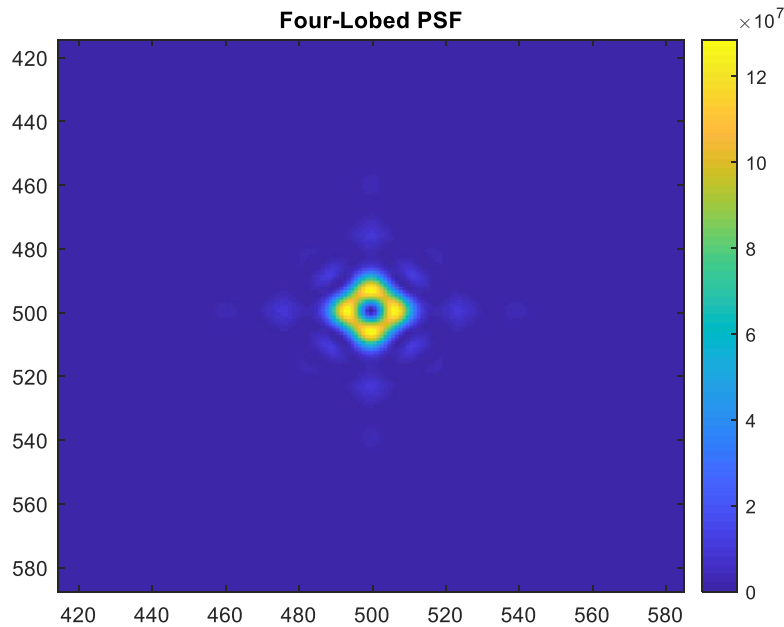


Figure 19. Diffraction limited four-lobed PSF at start of launch.

## 6. TRADE STUDY RESULTS

### 6.1 System Overview

The propagation model was used to examine the system’s radiometric response given several different combinations of input parameters. The two parameters that are varied from simulation to simulation are the initial projector beam power and therefore Strehl ratio, as given by Equation 24, and the beam PSF shape, which is given by one of the three options presented in Section 5.2. Three main Strehl ratios were tested: 50%, 70%, and 90%. Each of these was used when modeling all three of the beam PSF shapes. This gives a total of nine different system configurations modeled. For each Strehl ratio, the system performs the same from an AO perspective, regardless of beam PSF shape, because the power incident on the sail must always be  $P_b = 41$  GW at the starting projector-to-nanocraft distance. A summary of the power breakdown and AO performance in terms of residual wave-front variance and number of modes ( $N_m$ ) corrected is given by Table 5.

Table 5. Summary of AO performance and power breakdown.

Strehl Ratio (%)	Initial Power at Projector (GW)	Power Lost to Scattering/Absorption (GW)	Power Lost to Turbulence (GW)	Wave-Front Error in Correction ( $\text{rad}^2$ )	Number of Modes Corrected by AO
50	87.234	5.234	41	0.693	1.11E+08
70	62.32	3.739	17.581	0.357	2.38E+08
90	48.463	2.908	4.555	0.105	9.75E+08

The number of modes corrected is derived from the Noll approximation using Equation 44<sup>14</sup>. The key assumption made here is that the AO system perfectly corrects all scales larger than the specified sub-aperture diameter ( $D_{\text{sub}}$ ) of  $D_{\text{sub}} = 10$  m. Thus, the number of modes can be calculated using this diameter and then scaled up the actual projector diameter given by  $D_b = 4$  km. The Fried parameter ( $r_0$ ) is chosen to be  $r_0 = 0.2$  m. This number comes from recent Starshot estimations<sup>2</sup>. One might observe that the number of modes corrected here is not equal to the number of Zernike modes actually removed using the propagation model. The difference is that while the number of modes is indeed different, the resulting phase screen after Zernike removal was scaled via a user specified allowable wave-front variance that comes from the chosen Strehl ratio. This creates a wave-front that has the according error, just generated in a different way that is more advantageous from a processing time standpoint. In the real system it will obviously not be feasible to just scale the corrected wave-front, thus the actual number of corrected modes described in Table 5 is relevant.

$$N_m = \frac{D_b^2}{D_{sub}^2} \left( \frac{\sigma^2}{0.2944 \left( \frac{D_{sub}}{r_o} \right)^{\frac{5}{3}}} \right)^{\frac{-2}{\sqrt{3}}} \quad (44)$$

With the general system parameters set for each Strehl ratio configuration, the radiometric response from the individual beam PSF shapes can be outlined. Each PSF was sampled at ten evenly spaced projector-to-nanocraft distances throughout the launch duration.

## 6.2 Gaussian PSF

The incident power on the sail, as well as the power reflected back towards the projector, are plotted as a function of projector-to-nanocraft distance in Figure 20. The plots show the power in both scenarios for each of Strehl ratio as well. A Gaussian shaped PSF is considered here.

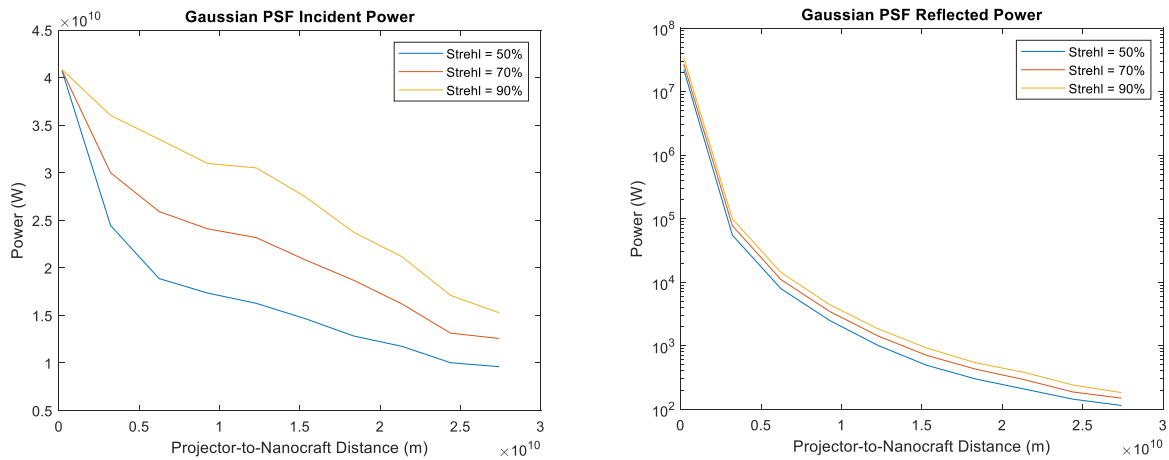


Figure 20. Incident and reflected power at several Strehl ratios for Gaussian PSF.

The plots show data that follows a relatively expected trend. In the case of both the incident and reflected beams, a higher Strehl ratio results in more power. In the case of the incident beam, the power falls off as the beam itself spills over the sail. However, the majority of the PSF core remains on the sail at all distances which limits the extent to which the power can decrease. When comparing these results to those from the kinematic model in Figure 6 it is important to note that these plots are given as a function of distance, while the plots in Figure 6 are given as a function of time. As a result, these plots appear to drop more rapidly as the projector-to-nanocraft distance does not vary linearly with time. This is the case for all trade study results.

The power reflected back towards the projector falls off much more dramatically, which is why it is plotted on a logarithmic axis. This has to do with the fact that the projector subtends a constantly decreasing solid angle at the sail. Thus, as the beam footprint on the sail expands, the rays begin to reflect at higher and higher angles of incidence. Because the BRDF is relatively specular, a majority of this power is then reflected away from the projector. Here, the largest contribution of reflected power comes the small portion of the expanded beam that hits the very center of the sail. The center of the sail is the closest to a flat mirror in shape, and thus the rays here are specularly reflected back towards the projector more than at larger projector-to-nanocraft distances. This is also why the reflected power is so much higher at the start of launch; the beam is most compact and at its smallest size here. A summary of the data is given in Table 6, where the initial and final values correspond to projector-to-nanocraft distances of  $z = 1.9e8$  m and at  $z = 2.7e10$  m respectively.

Table 6. Summary of incident and reflected power at several Strehl ratios for Gaussian PSF.

<b>Strehl Ratio (%)</b>	<b>Initial Incident Power (W)</b>	<b>Final Incident Power (W)</b>	<b>Initial Return Power (W)</b>	<b>Final Return Power (W)</b>
50	4.07E+10	9.61E+09	2.22E+07	114.286
70	4.08E+10	1.26E+10	2.72E+07	148.882
90	4.08E+10	1.53E+10	3.41E+07	181.819

Irradiance profiles for both the incident light and light reflected back towards the projector are provided at the initial, roughly middle, and final projector-to-nanocraft distances (i.e.  $z = 1.9e8$  m,  $1.2e10$  m, and  $2.7e10$  m) in Figure 21 when considering at Strehl of  $S = 50\%$ . The color bar is in units of Watts for all plots.

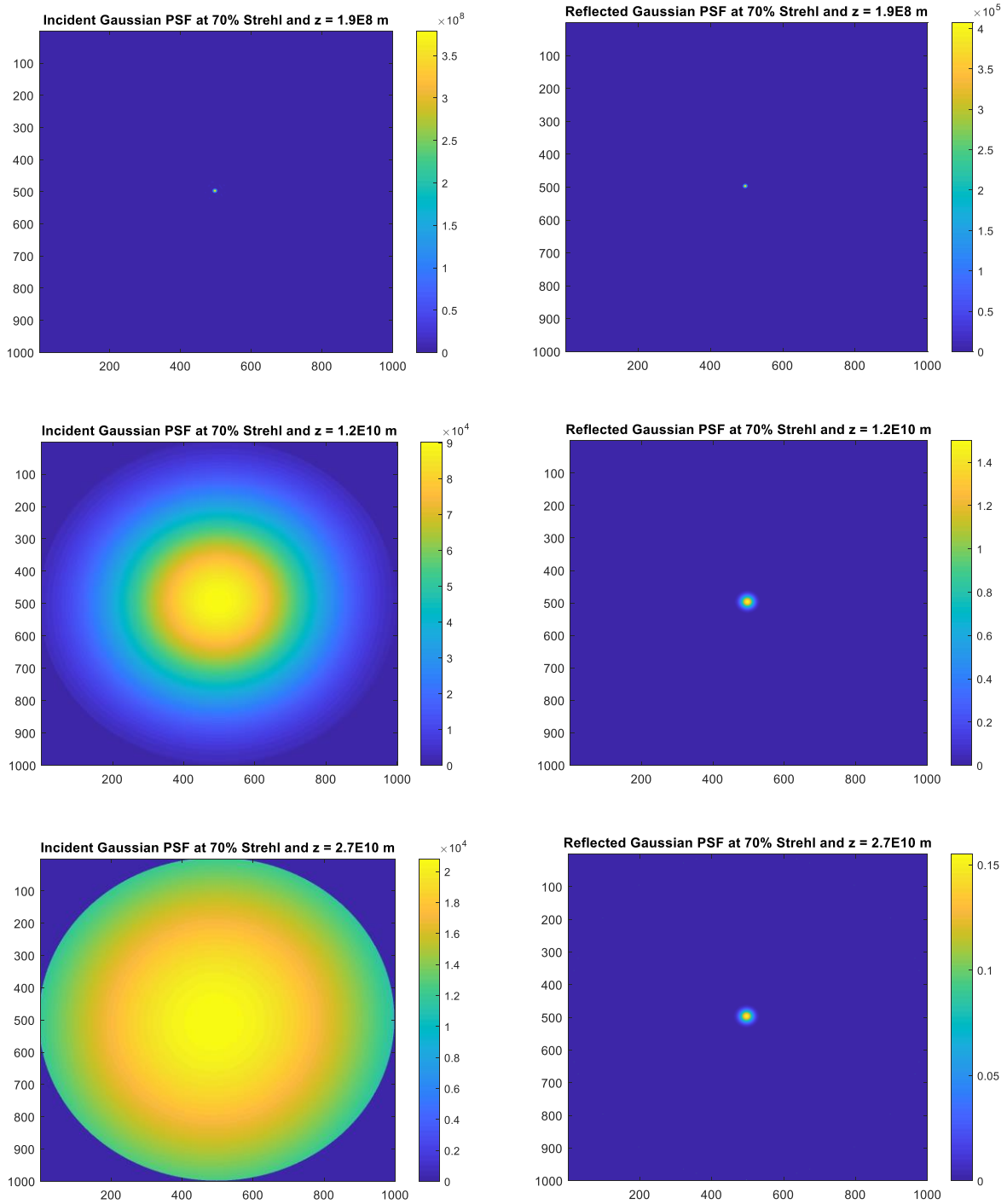


Figure 21. Incident and reflected irradiance profiles at 70% Strehl for Gaussian PSF.

The plots all reflect the data in Figure 20 and Table 6. The incident PSF is smallest at the start of launch and by the end has overfilled the sail. This results in less and less power reflected towards the projector, which causes a sharp drop in reflected power over the duration of launch. This is evidenced by the vast change in power per pixel between the initial and final reflected PSFs.

### 6.3 Donut PSF

The incident power on the sail, as well as the power reflected back towards the projector, are plotted as a function of projector-to-nanocraft distance in Figure 22. The plots show the power in both scenarios for each of Strehl ratio as well. A donut shaped PSF is considered here.

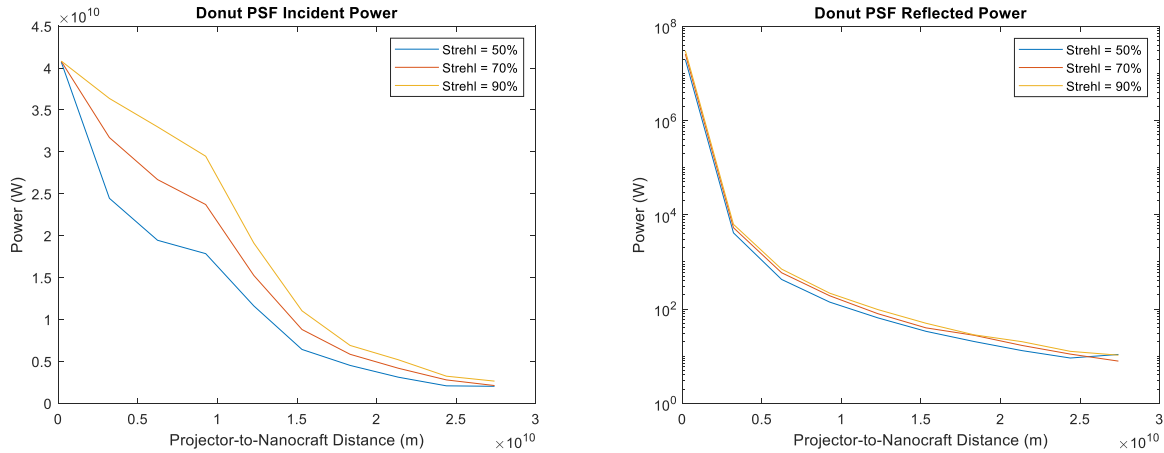


Figure 22. Incident and reflected power at several Strehl ratios for donut PSF.

The plots show data that follows similar trends to those provided in Section 6.2 for the Gaussian PSF. Once again, a higher Strehl ratio results in more power for both the incident and reflected beams. The reasoning for the drops in power is the same too. The notable difference between the two PSF responses is the magnitude of both the incident and reflected power.

At the majority of projector-to-nanocraft distances examined, the power is roughly an order of magnitude lower for the donut PSF than it is for the Gaussian PSF. This is likely due to the fact that the Gaussian has the majority of its power located at the beam's center, whereas the donut has heavy power concentration in a ring outside of the center. Thus, as the beam spills off of the sail the majority of the power falls off quicker in the case of the donut PSF. This leaves only the floor of the donut, which then continues to expand as well. Additionally, the donut PSF has a central spot size, defined as the distance from one edge of the ring to another, that is about 1.6 times the size of the Gaussian core. This means that the beam starts at an already expanded size when compared to the Gaussian. A summary of the data is given in Table 7, where the initial and final values correspond to projector-to-nanocraft distances of  $z = 1.9e8$  m and at  $z = 2.7e10$  m respectively.

Table 7. Summary of incident and reflected power at several Strehl ratios for donut PSF.

<b>Strehl Ratio (%)</b>	<b>Initial Incident Power (W)</b>	<b>Final Incident Power (W)</b>	<b>Initial Return Power (W)</b>	<b>Final Return Power (W)</b>
50	4.07E+10	2.02E+09	1.97E+07	10.88
70	4.08E+10	2.11E+09	2.57E+07	7.853
90	4.08E+10	2.64E+09	3.03E+07	10.496

Irradiance profiles for both the incident light and light reflected back towards the projector are provided at the initial, roughly middle, and final projector-to-nanocraft distances (i.e.  $z = 1.9e8$  m,  $1.2e10$  m, and  $2.7e10$  m) in Figure 23 when considering at Strehl of  $S = 50\%$ . The color bar is in units of Watts for all plots.

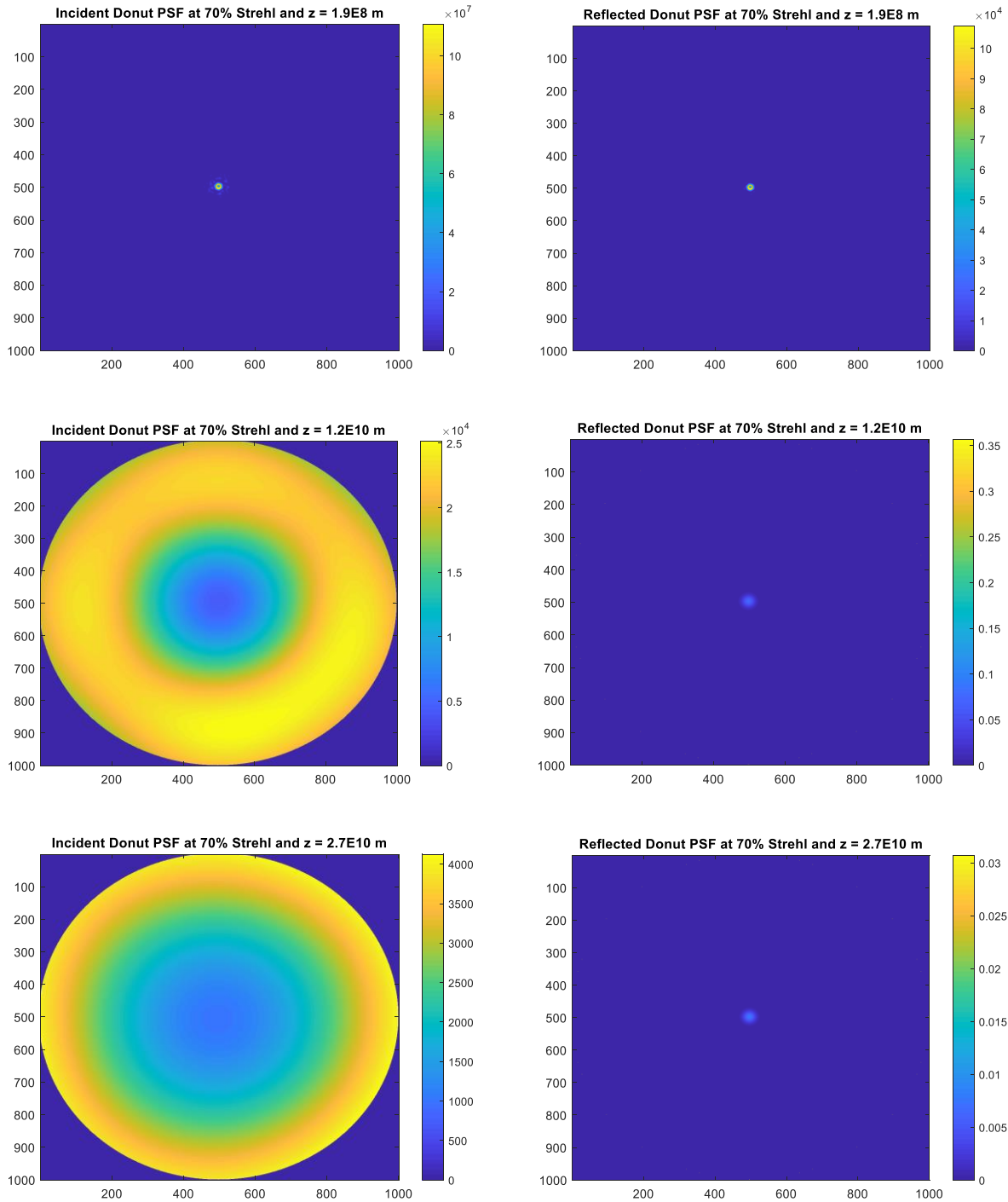


Figure 23. Incident and reflected irradiance profiles at 70% Strehl for donut PSF.

The plots are similar to those in Figure 21 in trend and reflect the data in Figure 22 and Table 7. The key difference between these plots and those in Figure 21 is the faintness of the return drive light at the largest projector-to-nanocraft distances. This derives from the fact that after the PSF overfills the sail, it is mostly the center of the floor that is being reflected.

## 6.4 Four-Lobed PSF

The incident power on the sail, as well as the power reflected back towards the projector, are plotted as a function of projector-to-nanocraft distance in Figure 24. The plots show the power in both scenarios for each of Strehl ratio as well. A four-lobed shaped PSF is considered here.

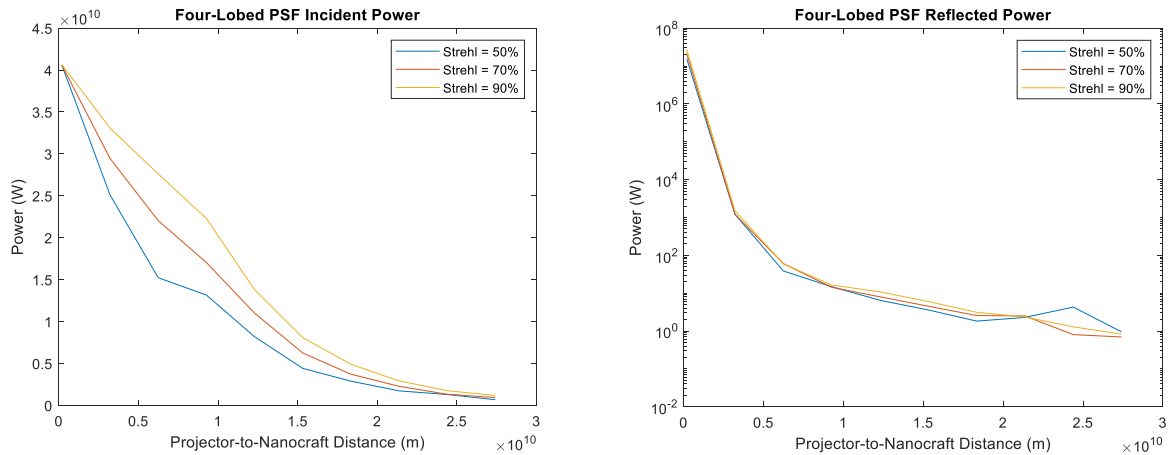


Figure 24. Incident and reflected power at several Strehl ratios for four-lobed PSF.

In general, the data here once again follows similar trends to those provided in Sections 6.2 and 6.3 for the Gaussian and donut PSFs. The higher Strehl ratio results in more power for both the incident and reflected beams and the power drops in the incident beam due to overfilling the sail and in the reflected beam due to higher angles of incidence.

At almost all projector-to-nanocraft distances the magnitude of both the incident and reflected power is approximately two orders of magnitude lower than the Gaussian and donut PSFs respectively. The reasoning for this difference is the same as with the donut PSF, except the four-lobed PSF has even less power concentrated in the center as there is no floor. Additionally, the four-lobed PSF has a central spot size, defined as the distance from the outer edge of one lobe to the outer edge of a lobe opposite about the beam's center, that is about 2 times the size of the Gaussian core. This spreads the incident beam footprint out even farther than in the case of the donut. The lack of center concentration coupled with the inherently larger beam size result in the least incident and reflected power of all three PSFs. A summary of the data is given in Table 8, where the initial and final values correspond to projector-to-nanocraft distances of  $z = 1.9e8$  m and at  $z = 2.7e10$  m respectively.

Table 8. Summary of incident and reflected power at several Strehl ratios for four-lobed PSF.

<b>Strehl Ratio (%)</b>	<b>Initial Incident Power (W)</b>	<b>Final Incident Power (W)</b>	<b>Initial Return Power (W)</b>	<b>Final Return Power (W)</b>
50	4.06E+10	6.76E+08	1.57E+07	0.949
70	4.06E+10	9.28E+08	2.15E+07	0.697
90	4.06E+10	1.17E+09	2.71E+07	0.829

Irradiance profiles for both the incident light and light reflected back towards the projector are provided at the initial, roughly middle, and final projector-to-nanocraft distances (i.e.  $z = 1.9e8$  m,  $1.2e10$  m, and  $2.7e10$  m) in Figure 25 when considering at Strehl of  $S = 50\%$ . The color bar is in units of Watts for all plots.

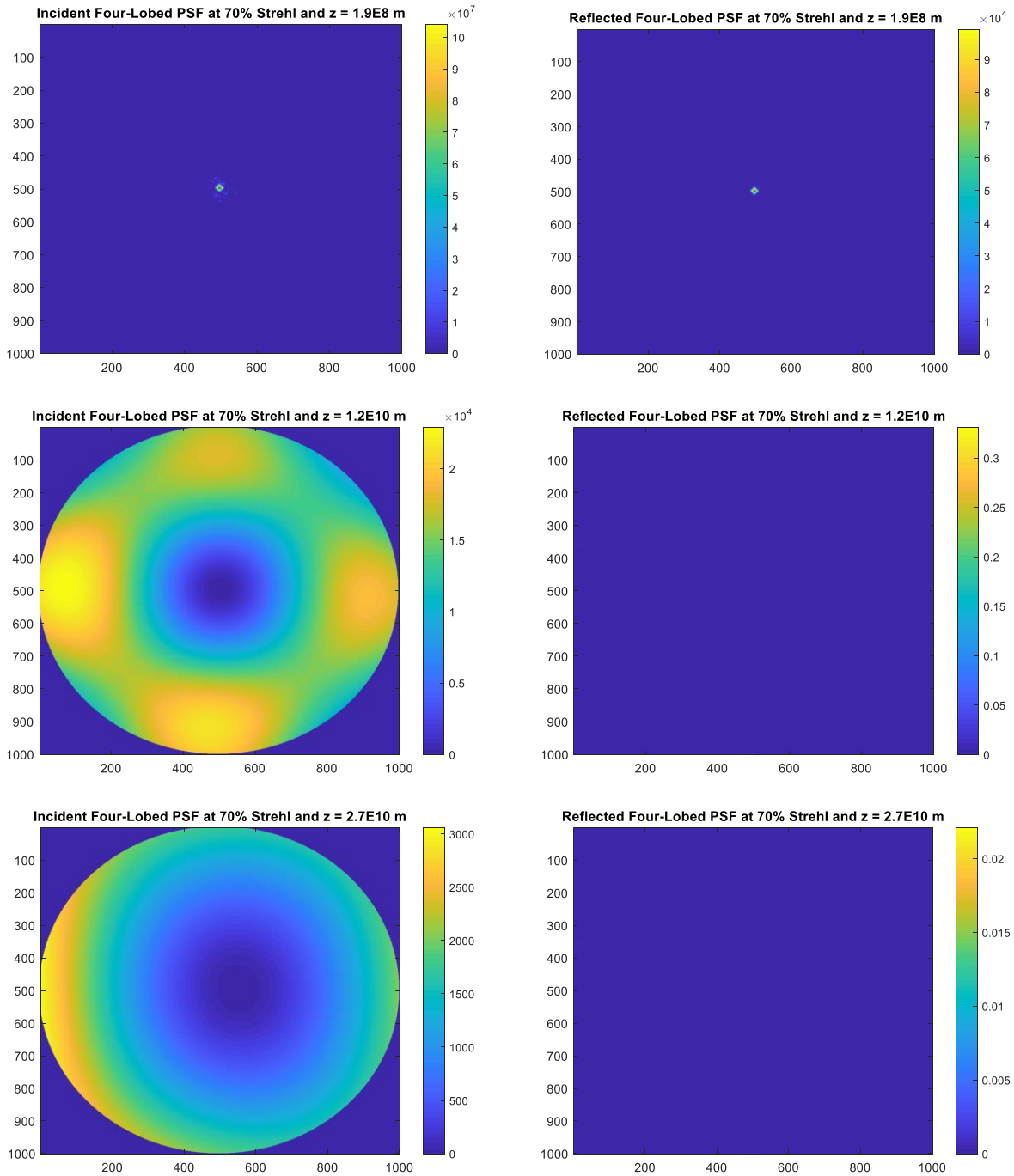


Figure 25. Incident and reflected irradiance profiles at 70% Strehl for four-lobed PSF.

As anticipated, the plots are similar to those in Sections 6.2 and 6.3, except at an order of magnitude less light. The return drive light is so low at the largest projector-to-nanocraft distances that the reflection is almost indistinguishable. The majority of the light here is coming from portions of the lobe edges, as there is little to no power concentrated in the center. This is reflected in the data in Figure 24 and Table 8.

## 6.5 Implications on System Design

The results presented in Sections 6.1-6.4 allow for an analysis on the potential for using the return drive light from the sail as a beacon. With Equation 45, the energy of a single return photon ( $E_{\text{photon}}$ ) can be calculated. The wavelength ( $\lambda$ ) used here is  $\lambda = 1074$  nm, which is Doppler shifted 10 nm from the original drive wavelength of  $\lambda_o = 1064$  nm. The Doppler shift used here is an estimate based on the fact that return drive light will not be used until 30 s into launch given the proposed guide beacon architecture. In reality, this wavelength will continue to Doppler shift throughout the duration of the launch, but the change is small enough in magnitude to have a minor impact on the results. Planck's constant ( $h$ ) is given as  $h = 6.626e-34$  m<sup>2</sup>kg/s while the speed of light ( $c$ ) is given as  $c = 2.998e8$  m/s.

$$E_{\text{photon}} = \frac{hc}{\lambda} \quad (45)$$

Using the minimum total power back at the projector (i.e. at the final distance of  $z = 2.7e10$  m) and an assumed atmospheric coherence time of  $\tau_o = 5$  ms the total number of photons ( $N_{\text{photon}}$ ) reflected back towards the projector in one full integration time is given by Equation 46. By using the minimum amount of power back, it can be inferred that the number of photons is only greater at all other distances, and thus this is the worst-case scenario.

$$N_{\text{photon}} = \frac{P_{\text{back}}\tau_o}{E_{\text{photon}}} \quad (46)$$

At this point, an assumption is used regarding the method of wave-front sensing. While the exact method is not yet determined, a Shack-Hartmann wave-front sensor has been proposed<sup>2</sup>. Using this style of wave-front sensing, the number of individual wave-front sensor sub-apertures (i.e. lenslets) can be assumed to be the number of modes corrected. The number of modes corrected is given as a function of Strehl ratio in Table 5. Assuming that the return light is collected evenly by each lenslet, Equation 47 is used to calculate the number of photons per sub-aperture ( $n$ ). Equation 48 then divides a full  $2\pi^2$  radians<sup>2</sup> over this number to calculate the wave-front variance of each measurement ( $\sigma_{\text{meas}}^2$ )<sup>14</sup>. It is assumed that the mean return wavelength ( $\lambda_A$ ) will be equal to the return wavelength of  $\lambda_o = 1074$  nm, rendering the ratio of wavelengths equal to unity.

$$n = \frac{N_{\text{photon}}}{N_m} \quad (47)$$

$$\sigma_{\text{meas}}^2 = \frac{2\pi^2}{n} \left( \frac{\lambda_A}{\lambda_o} \right) \quad (48)$$

Using this process with the data from each PSF shape at each Strehl, the wave-front variance of each measurement is calculated. Tables 9-11 display the results.

Table 9. Resulting wave-front error in measurement for Gaussian PSF.

<b>Gaussian PSF</b>		
<b>Strehl Ratio (%)</b>	<b>Final Return Power (W)</b>	<b>Wave-Front Error in Measurement (rad<sup>2</sup>)</b>
50	114.286	7.07E-10
70	148.882	1.17E-09
90	181.819	3.92E-09

Table 10. Resulting wave-front error in measurement for donut PSF.

<b>Donut PSF</b>		
<b>Strehl Ratio (%)</b>	<b>Final Return Power (W)</b>	<b>Wave-Front Error in Measurement (rad<sup>2</sup>)</b>
50	10.88	7.42E-09
70	7.853	2.22E-08
90	10.496	6.79E-08

Table 11. Resulting wave-front error in measurement for four-lobed PSF.

<b>Four-Lobed PSF</b>		
<b>Strehl Ratio (%)</b>	<b>Final Return Power (W)</b>	<b>Wave-Front Error in Measurement (rad<sup>2</sup>)</b>
50	0.949	8.51E-08
70	0.697	2.50E-07
90	0.829	8.59E-07

These results imply that the error in the wave-front measurement is always significantly less than the required error in the wave-front correction, as given in Table 5. This appears to hold true for all three PSF shapes at all three Strehl ratios. For a guide beacon to be of use to an AO system, the error in measurement must be less than the error in correction. Thus, this leads to the conclusion that the return drive light from the sail can indeed be utilized as a guide beacon for wave-front sensing purposes, given the system configurations investigated in this study.

Furthermore, the quality in AO correction has an impact on the amount of return drive light, but not so much so that it completely dictates the feasibility of using the return drive light as a beacon. It is important to note this can only be said of the regimes explored here (50%-90% Strehl). Under

this assumption, when designing the system one might weigh the cost of excess power vs. better AO correction and go with the cheaper option, even if the cheaper option is more power and less efficient AO. However, there are other factors to be considered that this study does not include. Arguably, one of the most pivotal of these is sail stability.

While a low Strehl may still provide enough return drive light for beacon use, it will still create a strong speckle pattern on the sail. This is evidenced in Figure 14. These random speckle fluctuations will result in random force distributions on the sail that could easily knock it off course. Therefore, it is likely that the system quality driving AO correction is not return drive light, but rather sail stability.

Another important metric to consider is the force on sail. While the model presented here quantifies return drive light, it does not quantify the exact nature of the force each ray imparts on the sail. While a Strehl of  $S = 50\%$  may be sufficient in terms of return drive light, the force resulting from such light is unlikely to be entirely along the desired line-of-sight. This is especially true as the beam footprint expands and the angles of incidence increase. Thus, additional light (i.e. more initial power or more efficient AO) may actually be required in order to successfully drive the sail in the allotted time of 600 s.

## **7. CONSIDERATIONS FOR FUTURE WORK AND CONCLUSIONS**

While the model here serves as a robust starting point, many additions can be made in the interests of future studies and simulations. In particular, the factors acknowledged in Section 6.5 are important to model. Both sail stability as well as force imparted in the direction of the nanocraft's line-of-sight are imperative to system success. One can imagine a scenario where the sail wobbles slightly as a result of force fluctuations. Not only would this be an obvious point of concern for sail stability, it may also lead to a speckle-like pattern of return drive light back at the projector. This would result in a return photon count that no longer depends only on the quantities modeled here, but on a more complex force distribution. In the current model, these fluctuations are not considered, but there are ongoing research efforts to examine these factors. Creating a

comprehensive model that incorporates all of these studies into one simulation would surely be of use to the project as a whole, and offer an expanded version of what Parkin has begun with his system model.

The current model can also continue to be used as a stand-alone model. Expanding upon the current architecture with more PSF shapes of interest, sail BRDFs, and many other system qualities could prove useful as new configurations are considered in the coming years. While Bowers has begun this process for BRDF and other drive space parameters, there is always room for improvement, particularly as new sail materials are proposed<sup>5</sup>. This holds true for the PSF shapes as well. For example, a study of how the return drive light varies with donut floor height could be of use. A floor equal to 20% the height of the peak was used here, but this is a far from settled number. The donut PSF is arguably the most feasible thus far, making this a useful area to explore. Additionally, while the beam was assumed to be focused at all projector-to-nanocraft distances for the purposes of this study, this is unlikely to be the case in the final system. Adding a defocus term to the PSF, particularly at the beginning of launch when the beam is most concentrated, has been proposed. If this is the case, the model will have to be edited to incorporate such a term.

The radiometric model presented has been used to successfully model both the nanocraft's kinematics, as well as the propagation of drive light to and from the sail, in an effort to quantify the amount of drive light returning to the projector given a variety of system configurations. Variations in both AO correction as well as PSF shape have been considered. The results conclude that over the course of launch, the return drive light can be used as a guide beacon. This is ideal for the guide beacon architecture proposed here, and likely serves as the best option available to the project for a wave-front sensing reference. The results are encouraging, and the model opens the door to further research efforts as well as overall system model integration. As a Phase 2 effort is considered, the conclusions here present considerations for system design as well as a path forward to further modeling the full scope of the Breakthrough Starshot Initiative.

## REFERENCES

- [1] Parkin, K., “The Breakthrough Starshot System Model,” Parkin Research, San Francisco, (2018).
- [2] Hart, M., “Wavefront Sensing for the Breakthrough Starshot Laser Launch Projector,” College of Optical Sciences, University of Arizona, (2017).
- [3] Noyes, M., “Orbital and Flight Stability Models for Breakthrough Starshot’s AO System,” College of Optical Sciences, University of Arizona, (2020).
- [4] Rice, J., “Preliminary Model for Radiometric Design and Analysis of the Breakthrough Starshot Initiative,” Proc. AO4ELT6, (2019).
- [5] Bowers, K. “Radiometric Modeling for Breakthrough Starshot: How Sail Shape and BRDF impact the Adaptive Optics,” College of Optical Sciences, University of Arizona, (2020).
- [6] Hyatt, J., “Laser Beam Projection for Starshot Launch,” Proc. AO4ELT6, (2019).
- [7] Kulkarni, N., “Relativistic Spacecraft Propelled by Directed Energy,” University of California Santa Barbara, (2017).
- [8] Goubau, G., Schwering, F., “On the guided propagation of electromagnetic wave beams,” IRE Transactions on Antennas and Propagation, 9(3), 248-256, (1961).
- [9] Noyes, M., “Analyzing the Viability of Satellite Laser Guide Stars for Breakthrough Starshot,” Proc. AO4ELT6, (2019).
- [10] Andrews, L., Phillips, R., “Laser Beam Propagation through Random Media, Second Edition,” SPIE Publishing, (2005).
- [11] Takato, N., Yamaguchi, I., “Spatial correlation of Zernike phase-expansion coefficients for atmospheric turbulence with finite outer scale,” Journal of the OSA, 12(5), 958-963, (1995).
- [12] Lane, R., Glindemann, A., and Dainty, J. C., “Simulation of a Kolmogorov Phase Screen,” Waves in Random Media 2, 209-224, (1992).
- [13] Reyes, J. et al., “Understanding optical changes in on-orbit spacecraft materials,” SPIE Optical Engineering and Applications, (2019).
- [14] Tyson, R., “Principles of Adaptive Optics,” CRC Press, (1991).